

The ISO-LWS map of the Serpens cloud core*

II. The line spectra

Bengt Larsson¹, René Liseau¹, and Alexander B. Men'shchikov^{1, 2}

¹ Stockholm Observatory, SCFAB, Roslagstullsbacken 21, SE-106 91 Stockholm, Sweden
e-mail: bem@astro.su.se, rene@astro.su.se

² Max-Planck-Institut für Radioastronomie, Auf dem Hügel, Bonn, Germany
e-mail: sasha@mpifr-bonn.mpg.de

Received date:

Accepted date:

Abstract. We present spectrophotometric ISO imaging with the LWS and the CAM-CVF of the Serpens molecular cloud core. The LWS map is centred on the far infrared and submillimetre source FIRS 1/SMM 1 and its size is $8' \times 8'$. The fine structure line emission in [O I] $63\text{ }\mu\text{m}$ and [C II] $157\text{ }\mu\text{m}$ is extended on the arcminute scale and can be successfully modelled to originate in a PDR with $G_0 = 15 \pm 10$ and $n(\text{H}_2)$ in the range of $(10^4 - 10^5)\text{ cm}^{-3}$. Extended emission might also be observed in the rotational line emission of H_2O and high- J CO. However, lack of sufficient angular resolution prevents us from excluding the possibility that the emission regions of these lines are point like, which could be linked to the embedded objects SMM 9/S 68 and SMM 4. Toward the Class 0 source SMM 1, the LWS observations reveal, in addition to fine structure line emission, a rich spectrum of molecular lines, superposed onto a strong, optically thick dust continuum (Larsson et al. 2000). The sub-thermally excited and optically thick CO, H_2O and OH lines are tracing an about 10^3 AU source with temperatures higher than 300 K and densities above 10^6 cm^{-3} ($M = 0.01 M_\odot$). The molecular abundances, $X = N(\text{mol})/N(\text{H}_2)$, are $X = (1, 0.1, 0.02, \geq 0.025) \times 10^{-4}$ for CO, H_2O , OH and ^{13}CO , respectively. Our data are consistent with an ortho-to-para ratio of 3 for H_2O . OH appears highly overabundant, which we tentatively ascribe to an enhanced (X-ray) ionisation rate in the Serpens cloud core ($\zeta \gg 10^{-18}\text{ s}^{-1}$). We show that geometry is of concern for the correct interpretation of the data and based on 2D-radiative transfer modelling of the disk/torus around SMM 1, which successfully reproduces the entire observed SED and the observed line profiles of low-to-mid- J CO isotopomers, we can exclude the disk to be the source of the LWS-molecular line emission. The same conclusion applies to models of dynamical collapse ('inside-out' infall). The $6''$ pixel resolution of the CAM-CVF permits us to see that the region of rotational H_2 emission is offset from SMM 1 by $30''$, at position angle 340° , which is along the known jet flow from the Class 0 object. This H_2 gas is extinguished by $A_V = 4.5$ mag and at a temperature of 10^3 K, which suggests that the heating of the gas is achieved through relatively slow shocks. Although we are not able to establish any firm conclusion regarding the detailed nature of the shock waves, our observations of the molecular line emission from SMM 1 are to a limited extent explainable in terms of an admixture of J-shocks and of C-shocks, the latter with speeds of about $(15-20)\text{ km s}^{-1}$, whereas dynamical infall is not directly revealed by our data.

Key words. ISM: individual objects: Serpens cloud core, FIRS 1/SMM 1 – abundances – molecules – clouds – jets and outflows – Stars: formation

1. Introduction

The Serpens dark cloud is currently forming a dense cluster of low to intermediate mass stars (Strom et al. 1976, Kaas 1999). This star forming complex is situated in the inner Galaxy, not very far from the direction to-

Send offprint requests to: B. Larsson

* Based on observations with ISO, an ESA project with instruments funded by ESA Member States (especially the PI countries: France, Germany, the Netherlands and the United Kingdom) and with the participation of ISAS and NASA.

ward the Galactic Centre ($\ell^{\text{II}} = 32^\circ$). At the distance of 310 pc (de Lara et al. 1991), the Serpens cloud core is only 30 pc from the nominal galactic plane, i.e. well within the scale height of the molecular gas of about 80 pc (Dame et al. 1987). Not totally unexpected, IRAS-observations revealed intense and patchy far infrared (FIR) emission on a sloping background. Earlier observations had discovered discrete FIR sources of relatively low luminosity (Nordh et al. 1982, Harvey et al. 1984).

The empirical classification scheme developed by Lada & Wilking (1984), and later extended by André et al. (1993), is based on the Spectral Energy Distribution (SED) of the young stellar objects. In a previous paper (Larsson et al. 2000), we were discussing the SEDs of the submm-sources in the Serpens cloud core and for the dominating source, SMM 1 (also known as Serpens FIRS 1; Harvey et al. 1984), we reached the conclusion that its SED classifies it as Class 0. The existence of a circumstellar disk has been announced by Brown et al. (2000). An immediate question is then, whether SMM 1 shows any detectable or deducable spectroscopic evidence of disk accretion and/or of dynamical infall. Over a 0.2 pc (about 2') region toward the Serpens cloud core, Williams & Myers (2000) reported signs of infall. Observations toward SMM 1 of molecular line profiles (Mardones et al. 1997) and Gregersen et al. (1997), have not so far been able to reveal a clear ‘collapse signature’. This is possibly because of confusion with the known mass outflow activity of the source (Rodríguez et al. 1989, Eiroa et al. 1992, McMullin et al. 1994, White et al. 1995, Davis et al. 1999, Williams & Myers 2000, Testi et al. 2000) and/or different velocity components in the could complex. On the other hand, Hogerheijde et al. (1999) found, from continuum interferometric observations, the density profile of the source to be consistent with the theoretical expectation of a collapsing cloud.

The earlier molecular line results were based on observations of low excitation transitions, which are not particularly (or not all) sensitive to the conditions expected to prevail in the deeper layers of the source. In this paper, we present spectral line data of the Serpens cloud core, both for a spatial map and for pointed deep integrations, which contain lines also of very high excitation. These are potentially better suited to ‘penetrate’ to regions which were previously hidden from view. Our interpretation of the results will especially focus on the evolution of this star forming complex.

In Sect. 2, we reiterate the LWS observations and a summary is given for the data reductions, whereas a more detailed account is provided in Appendix A. The resulting line spectra are presented in Sect. 3. These results are discussed at some depth in Sect. 4. We first exploit relatively simple analytical methods, which result in spatially averaged properties. These should be useful to limit the parameter space for more sophisticated numerical modelling. This is done for the transfer of both continuum and line radiation, and these models lead to some valuable conclusions. In a summarising discussion, we make an attempt to bring these various pieces of information into a coherent physical picture. Finally in Sect. 5, we summarise our main conclusions from this work.

2. Observations and data reductions

2.1. The ISO observations

A 5×5 spectrophotometric map in the far-infrared (FIR) of the Serpens cloud core was obtained with the Long-Wavelength Spectrometer (LWS; $43 - 197 \mu\text{m}$, $R_\lambda = 140 - 330$) on board the Infrared Space Observatory (ISO) on October 21, 1996. The ISO-project is described by Kessler et al. (1996) and the LWS is described by Clegg et al. (1996) and Swinyard et al. (1996).

The formal map centre, viz. $\alpha = 18^{\text{h}}29^{\text{m}}50^{\text{s}}29$ and $\delta = 1^\circ 15' 18''6$, epoch J 2000, coincides to within $10''$ with the position of the sub-millimetre source SMM 1. The pointing accuracy in the map is determined as $1''$ (rms). The spacings between positions in the map, oriented along the equatorial coordinates, are $100''$. The size of the LWS-map is $8' \times 8'$, corresponding to $(0.7 \times 0.7 = 0.5) D_{310}^2 \text{ pc}^2$, where D_{310} denotes the distance to the Serpens cloud core in units of 310 pc.

At each map-point the grating of the LWS was scanned 6 times in fast mode, oversampling the spectral resolution at twice the Nyquist rate. Each position was observed for nearly 15 min. The centre position was re-observed half a year later on April 15, 1997, for a considerably longer integration time (24 spectral scans).

In addition, imaging spectrophotometric data obtained with the Continuous Variable Filter (CVF; $5 - 16.5 \mu\text{m}$, $32 \times 32 \text{ pxl}$, $\text{pixel-FOV} = 6''$, $R_\lambda \gtrsim 35$) of ISO-CAM (Cesarsky et al. 1996) were also analysed. The detailed observing log is given in our previous paper (Larsson et al. 2000).

2.2. The reduction of the ISO data

2.3. LWS data

The LWS data reductions were done with the interactive analysis package LIA. This pipeline processing was done in two ways. For the long wave detectors LW1 – LW5, the Relative Spectral Response Functions (RSRFs) of the most recent version (OLP 10) provided an overall better agreement than the older OLP 8 for the detector intercalibration. However, the OLP 10 RSRFs also contained a number of strong features, which resulted in spurious ‘lines’ in the reduced spectra (Appendix A). We decided therefore to use the RSRFs of OLP 8, which did not show this behaviour, but scaled to the OLP 10 absolute levels. For the short-wave detectors SW1 – SW5, no such difference between OLP 8 and OLP 10 was apparent and consequently we used the latest version. A detailed account for the first steps in the LWS reduction is given in Appendix A.

Subsequent post-pipeline processing used the package ISAP. At each position, the individual LWS scans for each of the 10 detectors were examined, ‘deglitched’ and averaged. Corrections were applied to the ‘fringed’ spectra in the map. The fringing indicates that the emission is extended and/or that point sources were not on the optical

Table 1. Observed H₂ fluxes near SMM 1

Transition	Peak [†] (10 ⁻²¹ W cm ⁻²)	Total [‡] (10 ⁻²⁰ W cm ⁻²)
0-0 S(2)	2.9 ± 0.9	1.5 ± 0.2
0-0 S(3)	5.2 ± 0.6	4.8 ± 0.4
0-0 S(4)	8.8 ± 1.0	3.6 ± 0.3
0-0 S(5)	19.8 ± 1.2	7.0 ± 0.5
0-0 S(6)	6.2 ± 0.8	0.7 ± 0.2
0-0 S(7)	15.6 ± 2.8	5.8 ± 0.6
1-0 S(1) ^{II}	2.5	1.0

Notes to the table:

[†] Peak emission into a 36 arcsec² pixel.

[‡] Total emission over a source of 350 arcsec².

^{II} Estimated from Fig. 3 of Eiroa and Casali (1989).

axis of the LWS, i.e. the radial distance from the optical axis was typically larger than about 25''.

The absolute flux calibration is better than about 30% (Swinyard et al. 1996). Overlapping spectral regions of adjacent detectors were generally within 10% ('detector stitching' uncertainty). At 60 μm and 100 μm, the correspondance with broad-band IRAS data is even better than 10% (Larsson et al. 2000).

2.4. ISO-CAM-CVF data

The ISO-CAM data were reduced with the CIA programs using OLP8.4. This included dark current correction, transient correction and deglitching and flat field corrections. The calibrations were based on OLP 5.4. The proper alignment of the CVF fields was achieved with the aid of point sources identified in both CVF and broad-band (7 μm and 14 μm) CAM observations (Fig. 1).

3. Results

3.1. Spectral imaging in H₂

Lines from purely rotationally excited H₂ are clearly discernible in the CVF-image. In particular, all lines which fall in the observed spectral range, were detected and, in Table 1, their observed fluxes are listed. These refer to the 3 para-H₂ lines 0-0 S(2) 12.3, S(4) 8.0 and S(6) 6.1 μm and the 3 ortho-H₂ lines 0-0 S(3) 9.7, S(5) 6.9 and S(7) 5.5 μm. Fig. 2 shows maps near SMM 1 in these six lines, delineating the spatial distribution of the rotationally excited H₂ gas along the known jet-flow from SMM 1 (Eiroa & Casali 1989, Hodapp 1999). In addition, somewhat weaker H₂ emission is also observed near SMM 3, the discussion of which will be postponed to a future paper.

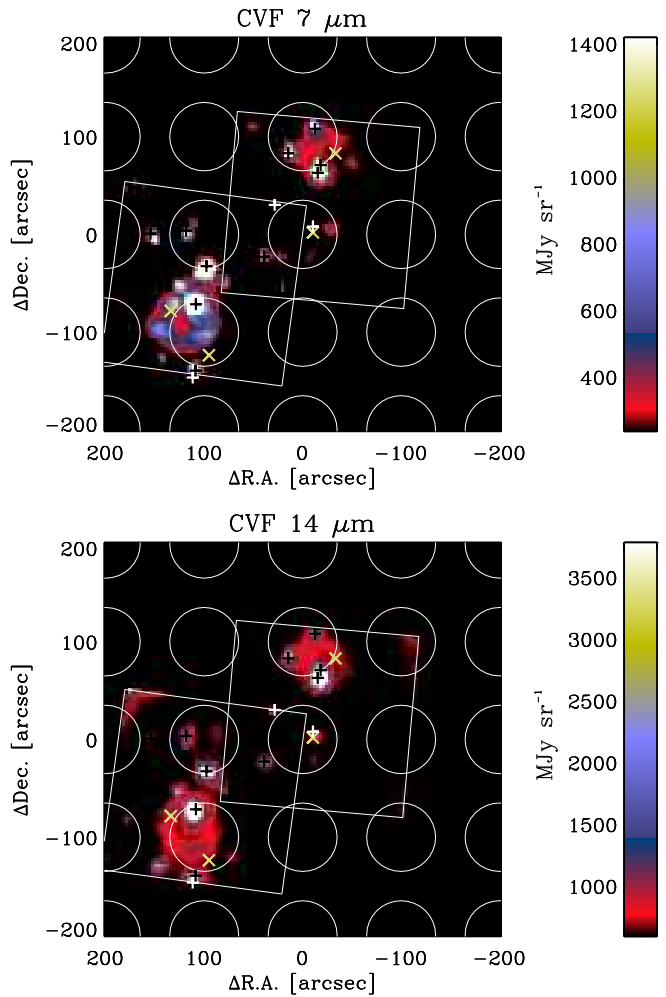


Fig. 1. The from CVF frames synthesised images at 7 μm and 14 μm. From comparison with CAM broad-band observations at these wavelengths and deep K-images the point sources were identified (see: Kaas 1999). These are shown by plus-signs (white and black) and were used to align the CVF frames with the equatorial coordinate system in the sky. Major SMM sources in the field are shown by yellow crosses. The LWS map pointings are indicated by the contours of the FWHM of the beam (white circles).

3.2. LWS-maps of [O I] 63 μm, [C II] 157 μm, ortho-H₂O 179.5 μm and CO 186 μm

Within the 8' × 8' map observed with the LWS, the spatial distribution of the fine structure lines [O I] 63 μm and [C II] 157 μm is shown in Fig. 3 together with that of the rotational lines of H₂O (2₁₂ – 1₀₁) (connecting to the ground state) and CO (J = 14 – 13) (lowest J-transition admitted and close in wavelength to the H₂O line).

Like the emission in [C II] 157 μm, [O I] 63 μm emission is observed in each position of our map, but with maximum intensity at the position of SMM 1. Secondary maxima are also seen along a ridge toward SMM 4/3/8 in the southeast-to-east. In addition, the emission is extended toward SMM 9/S 68 NW. The overall [O I] 63 μm distribu-

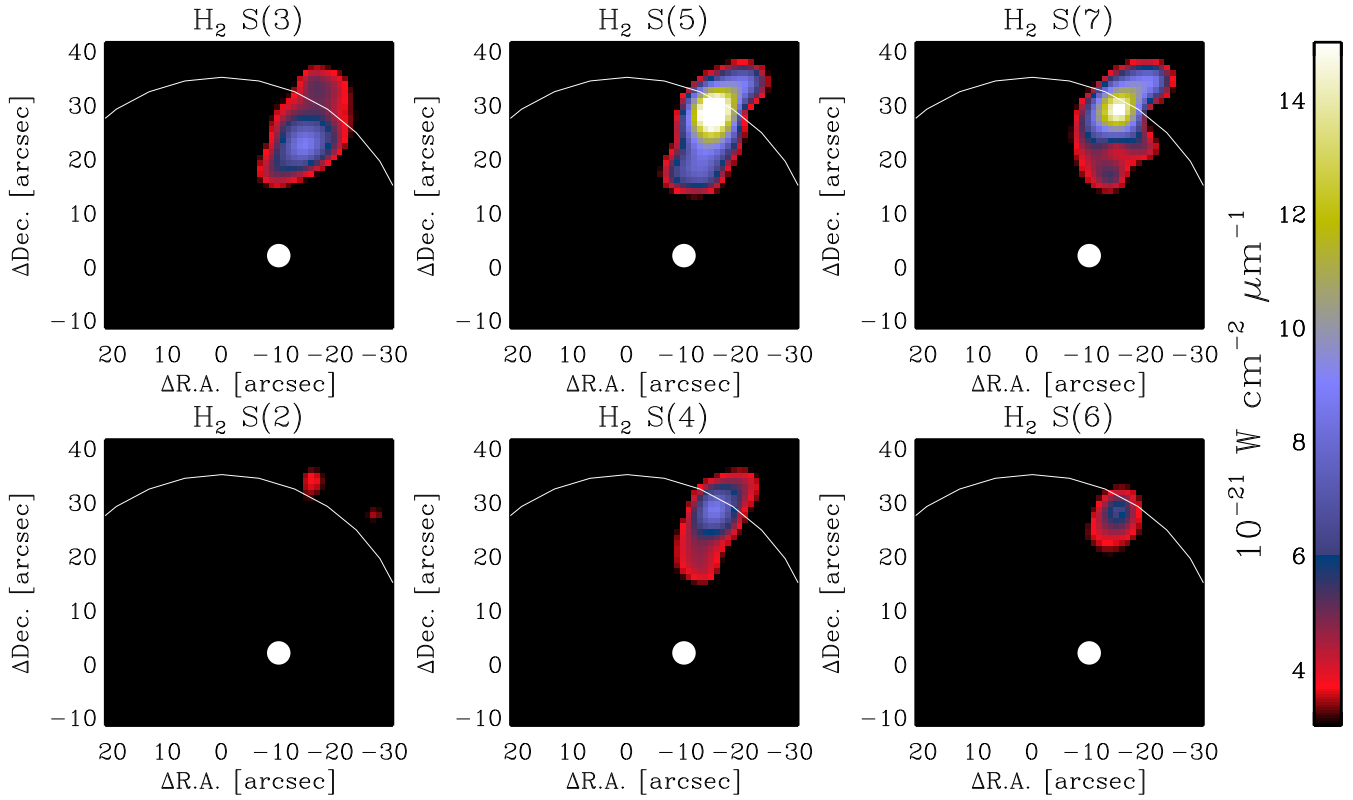


Fig. 2. CVF images toward SMM 1 in 3 ortho-H₂ (upper frames) and 3 para-H₂ (lower row) lines. Offsets are in arcsec and relative to the centre position (0, 0) of the LWS map. The white arcs outline the FWHM contour of the LWS beam (70'') and the white spot designates the position of SMM 1. The actual CVF pixels are square 6''.

tion is strikingly similar to that seen in the mm-regime in a variety of high density tracing molecules (McMullin et al. 2000). Very interesting is also the fact that, just in the northwest corner of the map, the shocked flow HH 460 (Davis et al. 1999, Ziener & Eislöffel 1999) seems to be discernible.

In [C II] 157 μm , maximum emission is seen toward S 68 (Sharpless 1959) and the cluster in the southeast, whereas SMM 1 is inconspicuous in this map. To some extent, the [C II] 157 μm -map is an inverted image of that seen in [O I] 63 μm .

The molecular emission in the 179.5 μm line of ortho-H₂O and in the 186 μm line of CO is strongest toward SMM 1, but displays also some extensions along the [O I] 63 μm ridge, i.e. toward the northwest and the southeast. The spatial resolution is not sufficient, however, to decide whether this emission is extended or due to the numerous SMM-sources in the region (cf. Fig. 3).

3.3. The line spectrum of SMM 1 from 43 to 197 μm

The continuum subtracted line spectrum of SMM 1 from 43 to 197 μm is displayed in Fig. 4, revealing a plethora of emission lines from both atomic and molecular species. In the figure, also the wavelength coverage of the ten individual LWS detectors is indicated (cf. Sect. 2.2). The identification of the lines and their parameters, as obtained from

profile fitting, are listed in Tables 2 to 5. Listed are the identified species, the upper and lower states and the rest wavelength of the transition. This is followed by the observed wavelength with the measurement error and the difference between the observed and the rest wavelength. Then the line width and the line flux with fitting-errors, respectively, are tabulated and the error estimate for the line flux, i.e. $\Delta F = \sqrt{\sigma_l^2 + \sigma_c^2}$ where σ_l is the fitting error and σ_c is the rms-level of the surrounding continuum integrated over one spectral resolution element. In the last two columns, the type of the Gauss fitting (single or multiple component) and the LWS detector are given.

Out of a total of 8 measured CO lines, clear detections are found for 7 transitions. In addition, we identify 5 (possibly 8) lines of ortho-H₂O, and 1 (possibly 2) of para-H₂O. Further, 4 lines of OH are clearly present in the spectrum, whereas for two more lines this status is less clear. Aside from the line emission from molecules, lines from O⁰ and C⁺ are also present. Possible implications from these results will be discussed in the following sections.

4. Discussion

4.1. The atomic line spectrum: CNO

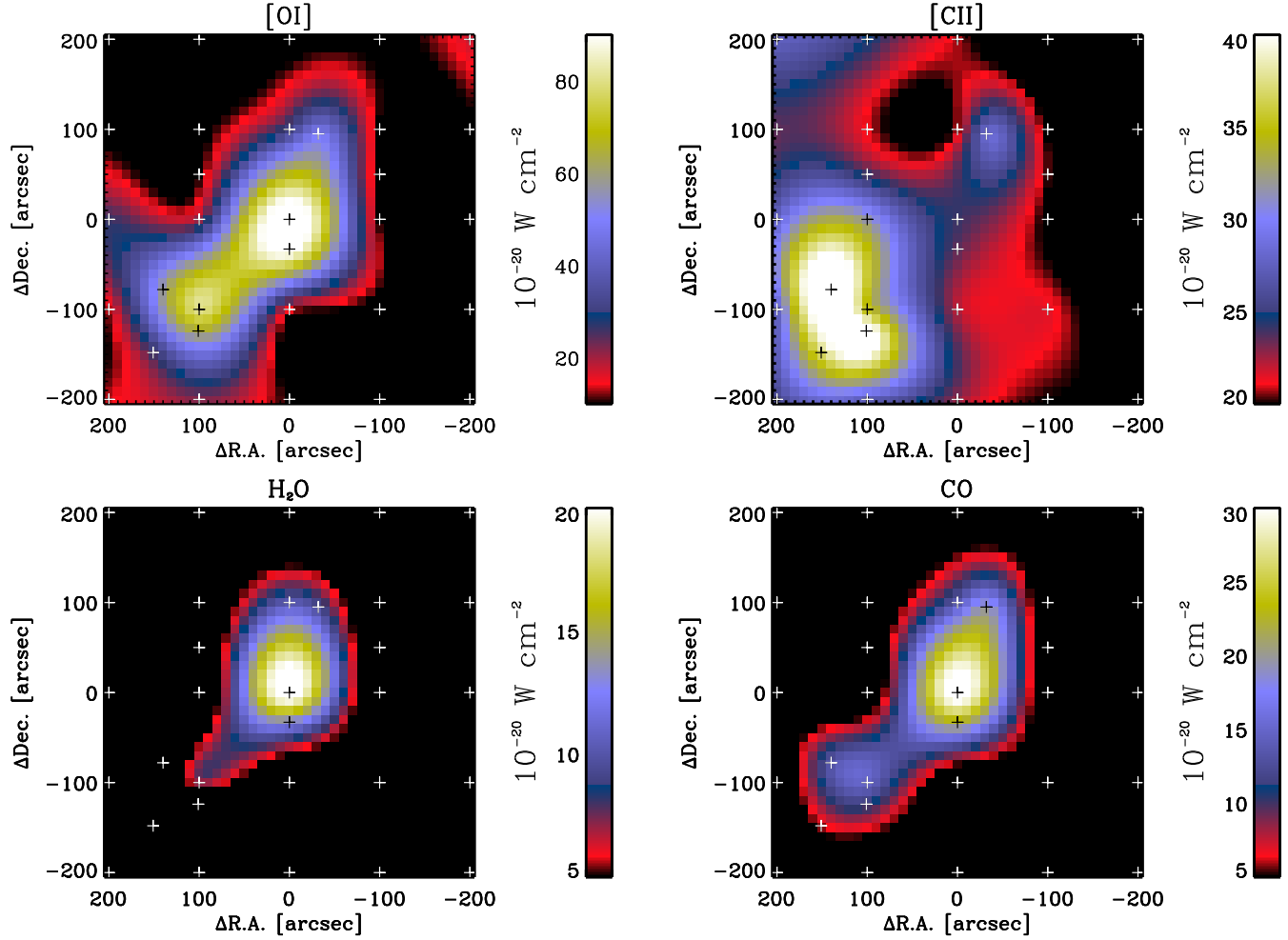


Fig. 3. Maps of integrated line fluxes of [OI] 63 μm , [C II] 157 μm , H₂O (2₁₂ – 1₀₁) and CO (14 – 13), with individual flux levels indicated by the bars next to each frame. The crosses refer to the positions toward which the LWS spectra have been obtained.

4.1.1. [O III] 53 μm , [O III] 88 μm and [N II] 122 μm

As is evident from Table 2, only upper limits were obtained for the high ionisation lines [O III] 53 μm , [O III] 88 μm and [N II] 122 μm . This is consistent with the luminosities derived by Larsson et al. (2000), indicating the presence of stellar sources generating at best only gentle UV-fields.

We can also exclude the presence of *extended* strongly shocked regions. For instance, if associated with the fast moving objects of Rodríguez et al. (1989), our data imply that the physical scales of these shocks would be small, $\ll 1''$ (e.g. for $v_s \sim 200 \text{ km s}^{-1}$ and $n_0 \gtrsim 10^5 \text{ cm}^{-3}$; see: Cameron & Liseau 1990; Liseau et al. 1996a).

We can conclude that the degree of ionisation of the atomic gas is generally low. Lines of low-ionisation species will be discussed in the next sections.

4.1.2. Extended emission: [C II] 157 μm and [OI] 63 μm

The spatial distribution of the [C II] 157 μm emission is shown in Fig. 3 from which it is evident that the emission varies within a factor of about two. The S68 nebulosity is

pronounced in the [C II] 157 μm line, making it likely that its origin is from a photodominated region (PDR), close to the cloud surface.

This idea can be tested quantitatively by invoking also the observed [OI] 63 μm emission. The LWS subtends a solid angle $\Omega_{\text{LWS}} = 9.0 \times 10^{-8} \text{ sr}$. Disregarding for a moment the peak emission (see below), we find for unit beam filling the line intensities $I_{157} = 2 \times 10^{-5} \text{ erg cm}^{-2} \text{ s}^{-1} \text{ sr}^{-1}$ and $I_{63} = 1 \times 10^{-5} \text{ erg cm}^{-2} \text{ s}^{-1} \text{ sr}^{-1}$, respectively. Hence, the line ratio [OI] 63 μm /[C II] 157 μm is about 0.5 (Fig. 5). These data are consistent with PDR-emission, where an interstellar radiation field about 10 times as intense as that of the solar neighbourhood, i.e. $G_0 \sim 10$, is impinging on the outer layers of a cloud with densities in the range $n(\text{H}) = (0.1 - 1) \times 10^5 \text{ cm}^{-3}$ (cf. Figs. 4 and 5 of Liseau et al. 1999). This estimate of the strength of the UV field is in reasonable agreement with the FIR-background measured by IRAS and ISO (Larsson et al. 2000), which would imply $G_0 = 5 - 25$. In the advocated PDR model, the [OI] 145 μm line is fainter by two orders of magnitude than the [OI] 63 μm line. The observed

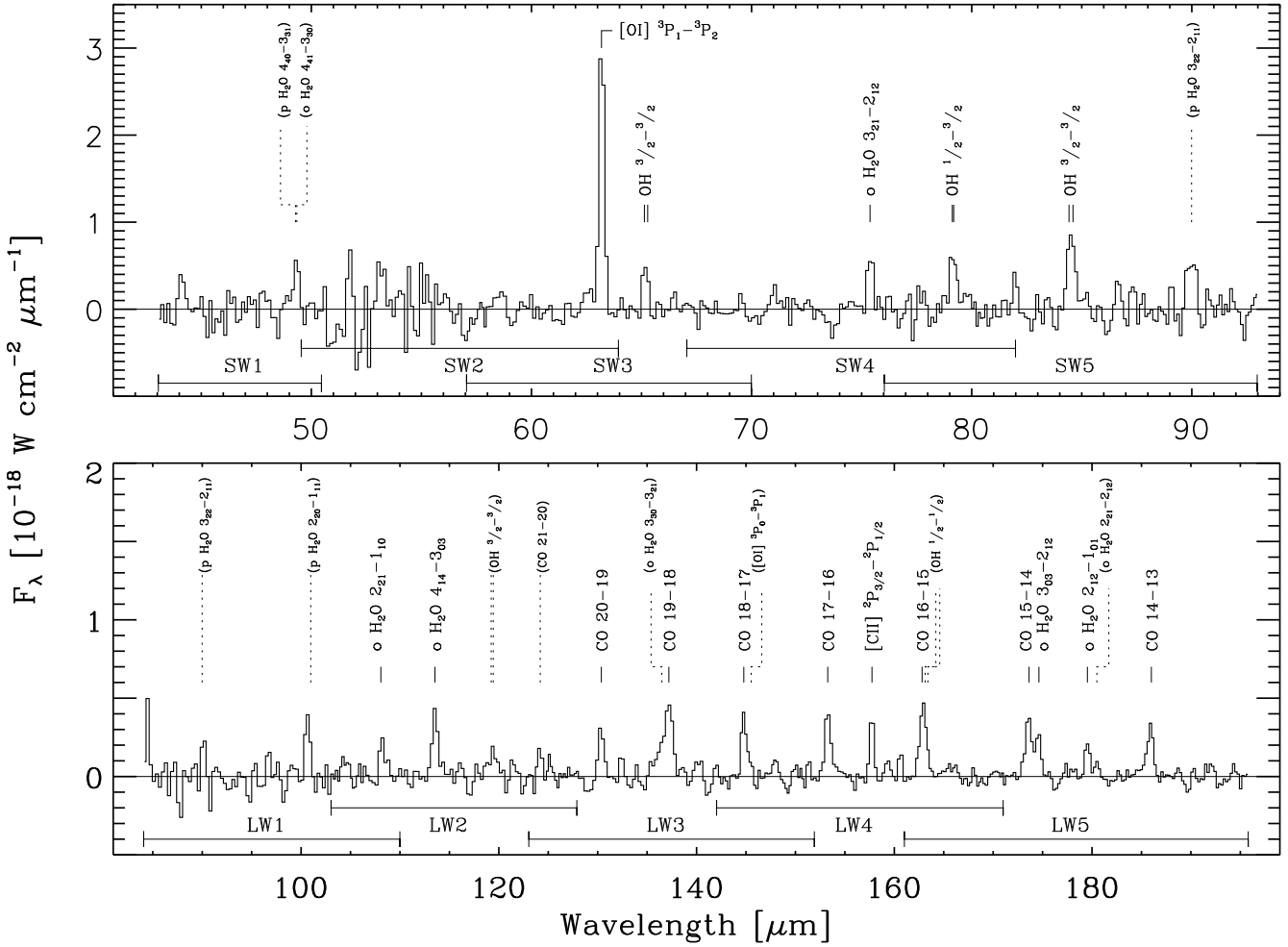


Fig. 4. The LWS spectrum (43 to 197 μm) of Serpens SMM 1 with line positions indicated. For clarity the strong continuum (Larsson et al. 2000) has been subtracted. The originally four times oversampled data have been rebinned to 0.1 μm for the short wavelength (SW) and to 0.2 μm for the long wavelength (LW) spectral range. Also shown, below the spectrum, is the extent of the individual LWS detectors.

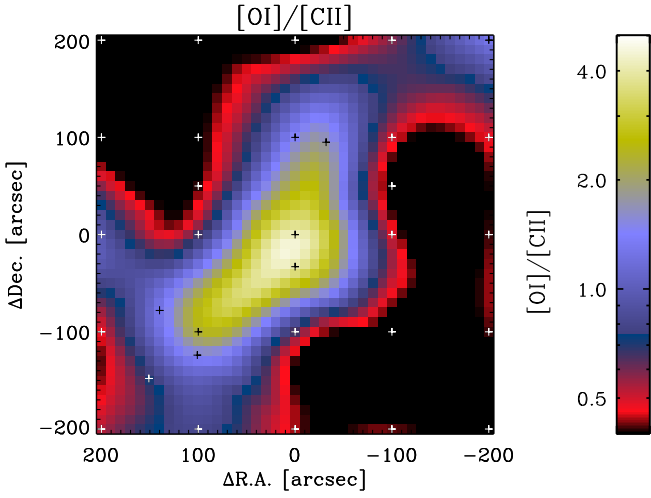


Fig. 5. Emission line intensity ratio map for [OI] 63 μm /[CII] 157 μm . Observed positions are identified by crosses. The observed flux distributions of the individual lines are shown in Fig. 3.

line ratio, $[\text{O I}] 63 \mu\text{m}/[\text{O I}] 145 \mu\text{m} > 12$, is clearly consistent with this prediction. Finally, no detectable emission from higher ionisation stages would be expected. The PDR model would offer therefore a satisfactory explanation for the observed fine structure line distribution over the map.

If this PDR emission is treated as a large scale background and subtracted from the maps, the resulting line ratio toward the peak (SMM 1) increases dramatically, viz. to $[\text{O I}] 63 \mu\text{m}/[\text{CII}] 157 \mu\text{m} = 15 \pm 5$. Such large ratios are generally not predicted by PDR models but are a common feature of J-shocks (Hollenbach & McKee 1989). The residual [OI] 63 μm flux corresponds to an observed intensity $I_{63} = 1 \times 10^{-4} \text{ erg cm}^{-2} \text{ s}^{-1} \text{ sr}^{-1}$, more than two orders of magnitude below that of J-shock models (see Sect. 4.1.3). Interpreted as a beam filling effect, this would imply the size of the shocked regions to be about 4'' to 5''.

Table 2. Line fluxes of atoms and ions toward SMM 1

Ion id	Transition	Wavelength (μm)				Flux $\times 10^{19}$ (W cm^{-2})	Single/ Multi fit	LWS Detector
		λ	λ_{obs}	$\Delta\lambda$	σ_{λ}			
[CII]	${}^2\text{P}_{3/2} - {}^2\text{P}_{1/2}$	157.74	157.72 ± 0.02	-0.02	0.46 ± 0.03	2.07 ± 0.21	0.35	S LW 4
			157.72 ± 0.04	-0.02	0.60 Fix	2.31 ± 0.20	0.34	S LW 4
[OI]	${}^3\text{P}_0 - {}^3\text{P}_1$	145.53	145.53 Fix	+0.00	0.60 Fix	0.37 ± 0.84	0.90	M LW 4
			145.53 Fix	+0.00	0.60 Fix	0.76 ± 0.83	0.89	M LW 3
	${}^3\text{P}_1 - {}^3\text{P}_2$	63.18	63.19 ± 0.01	+0.01	0.27 ± 0.01	9.5 ± 0.7	0.74	S SW 3
			63.19 ± 0.01	+0.01	0.29 Fix	9.8 ± 0.4	0.46	S SW 3
[NII]	${}^3\text{P}_2 - {}^3\text{P}_1$	121.90	63.17 ± 0.01	-0.01	0.28 ± 0.01	10.3 ± 0.9	0.96	S SW 2
			63.17 ± 0.01	-0.01	0.29 Fix	10.5 ± 0.5	0.60	S SW 2
	${}^3\text{P}_1 - {}^3\text{P}_0$	88.36				0.29	S LW 2	
						0.47	S LW 1	
[OIII]	${}^3\text{P}_2 - {}^3\text{P}_1$	51.82				0.32	S SW 5	
						0.73	S SW 2	

4.1.3. The [OI] 63 μm emission toward HH 460

Toward the interstellar shock, HH 460, the [OI] 63 μm flux is not conspicuously larger than that of [CII] 157 μm , as one might naively expect for shock excitation, and we cannot exclude the possibility that the spatial coincidence with the [OI] 63 μm emission spot is merely accidental. However, pursuing the shock idea we find that, for the previously inferred cloud densities, $\gtrsim 10^5 \text{ cm}^{-3}$, the [OI] 63 μm intensity is roughly constant with the shock speed (a few times $10^{-2} \text{ erg cm}^{-2} \text{ s}^{-1} \text{ sr}^{-1}$; Hollenbach & McKee 1989). These J-shock models do also predict that the accompanying [OI] 145 μm emission would not be detectable in our observations and that any [CII] 157 μm contribution would be totally insignificant.

The observed line intensity is $1 \times 10^{-5} \text{ erg cm}^{-2} \text{ s}^{-1} \text{ sr}^{-1}$ which, if due to shock excitation, would indicate that the source fills merely a tiny fraction of the LWS-beam (beam dilution of 2.5×10^{-4}). A size of about 1" for the [OI] 63 μm emitting regions of the HH object would thus be implied, which is comparable to the dimension of the dominating, point-like, optical knot HH 460 A. From the observed line flux, a current mass loss rate from the HH-exciting source of $\dot{M}_{\text{loss}} = 3 \times 10^{-7} M_{\odot} \text{ yr}^{-1}$ would be indicated (Hollenbach 1985, Liseau et al. 1997), which is at the 3% level of the mass accretion rate in the Serpens cloud core (Sect. 4.4).

Based on the $L_{63} - L_{\text{bol}}$ calibration by Liseau et al. (1997), one would predict that the luminosity of the central source is slightly less than $0.5 L_{\odot}$. No detailed information about the exciting source of HH 460 is available, though. Based entirely on morphological arguments, Ziener & Eislöffel (1999) associate HH 460 with SMM 1, and Davis et al. (1999) either with SMM 1 or with SMM 9/S 68N. The inferred luminosities of these objects, $71 L_{\odot}$ and $16 L_{\odot}$, respectively (Larsson et al. 2000), are however much larger than that inferred for the putative source driving HH 460. Evidently, the present status regarding the identification of the driving source of HH 460

is inconclusive. Proper motion and radial velocity data would be helpful in this context.

4.2. H_2 , CO, H_2O and OH toward SMM 1

We can directly dismiss the PDR of Sect. 4.1.2 as responsible for the molecular line emission observed with the LWS, since gas densities and kinetic temperatures are far too low for any significant excitation of these transitions. Shock excitation would be an obvious option. In the following, we will examine the line spectra of H_2 , CO, H_2O and OH.

4.2.1. Rotation diagram: H_2 and CO

The analytical technique known as ‘rotation diagram’ analysis is relatively simple and easy to apply to wavelength integrated molecular rotational line data. The advantages and the shortcomings of this analysis tool have been thoroughly discussed by Goldsmith & Langer (1999).

Assuming the lines to be optically thin and to be formed in Local Thermodynamic Equilibrium (LTE), one can derive the equation of a straight line for the molecular column density as a function of the upper level energy in temperature units. The slope of this line is the reciprocal excitation temperature of the levels (which in LTE is the same for all levels and equals the kinetic gas temperature), viz.

$$\ln \left(\frac{4\pi}{h\nu_0 g_u A_{\text{ul}}} \frac{\int_{\text{line}} F_{\lambda} d\lambda}{\Omega_{\text{beam}}} \right) = \ln \left(\frac{N_{\text{mol}}}{Q(T_{\text{ex}})} \right) - \frac{E_u}{kT_{\text{ex}}} \quad (1)$$

where the symbols have their usual meaning. The left hand side of Eq. (1) entails the column density of the molecules in the upper levels. For H_2 , the upper level energies, E_u , were obtained from Abgrall & Roueff (1989) and the Einstein transition probabilities, A_{ul} , were adopted from Wolniewicz et al. (1998). For CO, these data were taken from Chandra et al. (1996). The statistical weights of the upper levels are given by $g_u = (2I + 1)(2J_u + 1)$, where

Table 3. CO line measurements in the spectrum of SMM 1

Transition ($J \rightarrow J - 1$)	Wavelength (μm) λ_{obs}	Width (μm) $\Delta\lambda$	Flux $\times 10^{19}$ (W cm^{-2}) F	Err $\times 10^{19}$ (W cm^{-2}) ΔF	Single/ Multi fit	LWS Detector		
14 – 13	186.00	185.88 \pm 0.03	–0.12	0.76 \pm 0.03	<u>2.64 \pm 0.30</u>	0.37	S	LW 5
		185.90 \pm 0.03	–0.10	0.60 Fix	<u>2.32 \pm 0.16</u>	0.27	S	LW 5
15 – 14	173.63	173.60 \pm 0.03	–0.03	0.81 \pm 0.03	3.34 \pm 0.28	0.35	S	LW 5
		173.59 \pm 0.03	–0.04	0.60 Fix	2.81 \pm 0.21	0.30	S	LW 5
16 – 15	162.81	162.90 \pm 0.02	+0.09	0.98 \pm 0.02	<u>4.58 \pm 0.19</u>	0.28	S	LW 5
		162.92 \pm 0.04	+0.12	0.60 Fix	3.38 \pm 0.34	0.40	S	LW 5
		162.81 Fix		0.60 Fix	<u>2.67 \pm 0.50</u>	0.54	M	LW 5
		162.93 \pm 0.02	+0.12	0.59 \pm 0.02	3.19 \pm 0.18	0.36	S	LW 4
		162.93 \pm 0.04	+0.12	0.60 Fix	3.21 \pm 0.10	0.33	S	LW 4
17 – 16	153.27	153.28 \pm 0.02	+0.01	0.64 \pm 0.02	<u>2.81 \pm 0.20</u>	0.34	S	LW 4
		153.27 \pm 0.02	+0.00	0.60 Fix	2.71 \pm 0.11	0.30	S	LW 4
18 – 17	144.78	144.73 \pm 0.02	–0.05	0.57 \pm 0.03	2.55 \pm 0.31	0.44	S	LW 4
		144.75 \pm 0.03	–0.03	0.60 Fix	2.63 \pm 0.16	0.36	S	LW 4
		144.78 Fix		0.60 Fix	<u>2.50 \pm 0.22</u>	0.39	M	LW 4
		144.78 \pm 0.02	+0.00	0.50 \pm 0.02	2.67 \pm 0.28	0.42	S	LW 3
		144.79 \pm 0.03	+0.01	0.60 Fix	<u>2.94 \pm 0.23</u>	0.38	S	LW 3
19 – 18	137.20	137.19 \pm 0.03	–0.01	0.80 \pm 0.04	3.39 \pm 0.41	0.53	S	LW 3
		137.21 \pm 0.04	+0.01	0.60 Fix	2.85 \pm 0.28	0.43	S	LW 3
		137.20 Fix		0.60 Fix	<u>2.83 \pm 0.30</u>	0.45	M	LW 3
20 – 19	130.37	130.35 \pm 0.03	–0.02	0.68 \pm 0.03	2.48 \pm 0.32	0.48	S	LW 3
		130.34 \pm 0.03	–0.03	0.60 Fix	<u>2.33 \pm 0.18</u>	0.39	S	LW 3
21 – 20	124.19	124.21 \pm 0.05	+0.02	0.48 \pm 0.06	0.98 \pm 0.32	0.48	S	LW 3
		124.20 \pm 0.08	+0.01	0.60 Fix	<u>1.08 \pm 0.23</u>	0.42	S	LW 3
		124.10 \pm 0.05	–0.09	0.52 \pm 0.06	1.17 \pm 0.31	0.42	S	LW 2
		124.10 \pm 0.06	–0.09	0.60 Fix	<u>1.25 \pm 0.18</u>	0.34	S	LW 2
22 – 21	118.58					0.29	S	LW 2

Notes to the table:

$\Delta F = \sqrt{\sigma_1^2 + \sigma_c^2}$ where σ_1 is the fitting error and σ_c is the rms-level of the surrounding continuum integrated over one spectral resolution element, i.e. 0.29 μm and 0.60 μm for the SW and LW detectors, respectively. S = Single line component fit; M = multi component line fit. Underlined flux values were used in the rotation diagram analysis and are shown in Fig. 7.

I is the quantum number of the nuclear spin. Further, for the evaluation of the approximate partition function

$$Q(T_{\text{ex}}) \approx \frac{k T_{\text{ex}}}{h c B_0} \quad (2)$$

we used the rotational constant, $B_0 = 59.33451 \text{ cm}^{-1}$, for H_2 from Bragg et al. (1982). For CO, $B_0 = 1.9225 \text{ cm}^{-1}$, was obtained from the data by Lovas et al. (1979). Graphs of Eq. (1) are shown in Figs. 6 and 7, fitted to the CAM-CVF and LWS data, respectively.

To obtain a consistent result, the H_2 data need to be corrected for the foreground extinction. Using the data of Ossenkopf & Henning (1994; model for thin ice coating, $n = 10^5 \text{ cm}^{-3}$, $t = 10^5 \text{ yr}$), an extinction correction of $A_V = 4.5 \text{ mag}$ resulted in a total column density of warm H_2 gas of $N(\text{H}_2) = (9.5 \pm 2.0) \times 10^{18} \text{ cm}^{-2}$. The rotation temperature is $T_{\text{ex}} = (1060 \pm 100) \text{ K}$ and an ortho-to-para ratio (nuclear spin state population) of $o/p = 3$ is implied by these data.

In Fig. 7, ground-based CO data from the literature were added for lower lying transitions. Evidently, the high- J distribution appears markedly different from that of the low- J lines. If these latter lines were truly optically thin, they could originate in extended cloud gas, where $T_{\text{low-}J} = (62 \pm 6) \text{ K}$, of column density $N_{\text{low-}J} = (2.0 \pm 0.2) \times 10^{17} \text{ cm}^{-2}$. Seemingly in contrast, the LWS data identify gas at a characteristic temperature of $T_{\text{high-}J} = (320 \pm 20) \text{ K}$, with an LTE-column density of $N_{\text{high-}J} = (1.9 \pm 0.2) \times 10^{15} \text{ cm}^{-2}$.

These results are based on ad hoc assumptions, i.e. that of unit beam filling and of low optical depth in the lines, potentially underestimating the column densities, and that the level populations are distributed according to their LTE values. LTE may be a reasonably good assumption for the low- J lines. Regarding CO, it is however questionable to what extent these are optically thin. On the other hand, low opacity may come close to the truth for the high- J lines, but LTE is not at all guaranteed a priori for these transitions. Obviously, one needs to check

Table 4. H₂O line measurements in the spectrum of SMM 1

Transition		Wavelength	Width	Flux $\times 10^{19}$	Err $\times 10^{19}$	Single/	LWS
		(μm)	(μm)	(W cm^{-2})	(W cm^{-2})	Multi	Detector
	λ	λ_{obs}	$\Delta\lambda$	σ_λ	F	fit	
<u>ortho-H₂O</u>							
2 ₂₁ – 2 ₁₂	180.49	180.49 \pm 0.03	+0.00	0.45 \pm 0.03	0.53 \pm 0.11	S	LW 5
		180.49 \pm 0.05	+0.00	0.60 Fix	0.60 \pm 0.01	S	LW 5
2 ₁₂ – 1 ₀₁	179.53	179.55 \pm 0.04	+0.02	0.57 \pm 0.04	1.40 \pm 0.24	S	LW 5
		179.55 \pm 0.04	+0.02	0.60 Fix	1.43 \pm 0.13	S	LW 5
3 ₀₃ – 2 ₁₂	174.63	174.63 \pm 0.03	+0.00	0.70 \pm 0.03	2.15 \pm 0.24	S	LW 5
		174.63 \pm 0.03	+0.00	0.60 Fix	1.97 \pm 0.14	S	LW 5
		174.63 \pm 0.06	+0.00	0.60 Fix	1.93 \pm 0.66	M	LW 5
3 ₃₀ – 3 ₂₁	136.49	136.52 \pm 0.09	+0.03	0.64 \pm 0.11	0.85 \pm 0.34	S	LW 3
		136.51 \pm 0.06	+0.02	0.60 Fix	0.81 \pm 0.11	S	LW 3
		136.51 Fix	+0.02	0.60 Fix	0.77 \pm 0.82	M	LW 3
4 ₁₄ – 3 ₀₃	113.54	113.54 \pm 0.04	+0.00	0.61 \pm 0.04	2.96 \pm 0.39	S	LW 2
		113.54 \pm 0.03	+0.00	0.60 Fix	2.93 \pm 0.21	S	LW 2
2 ₂₁ – 1 ₁₀	108.07	108.13 \pm 0.05	+0.06	0.39 \pm 0.02	1.29 \pm 0.40	S	LW 2
		108.18 \pm 0.07	+0.11	0.60 Fix	1.58 \pm 0.31	S	LW 2
		107.83 \pm 0.03	-0.25	0.51 \pm 0.05	1.60 \pm 0.24	S	LW 1
		107.84 \pm 0.05	-0.24	0.60 Fix	1.79 \pm 0.22	S	LW 1
3 ₂₁ – 2 ₁₂	75.38	75.40 \pm 0.03	+0.02	0.29 \pm 0.03	2.05 \pm 0.51	S	SW 4
		75.40 \pm 0.03	+0.02	0.29 Fix	2.03 \pm 0.28	S	SW 4
4 ₄₁ – 3 ₃₀	49.34	49.32 \pm 0.02	-0.02	0.25 \pm 0.02	1.69 \pm 0.29	S	SW 1
		49.32 \pm 0.02	-0.02	0.29 Fix	1.81 \pm 0.18	M	SW 1
<u>para-H₂O</u>							
2 ₂₀ – 1 ₁₁	100.98	100.66 \pm 0.05	-0.32	0.57 \pm 0.04	2.53 \pm 0.68	S	LW 1
		100.66 \pm 0.06	-0.32	0.60 Fix	2.60 \pm 0.37	S	LW 1
3 ₂₂ – 2 ₁₁	89.99	89.99 \pm 0.05	+0.00	0.44 \pm 0.04	2.71 \pm 0.76	S	SW 4
		90.01 \pm 0.04	+0.02	0.29 Fix	2.02 \pm 0.42	S	SW 4

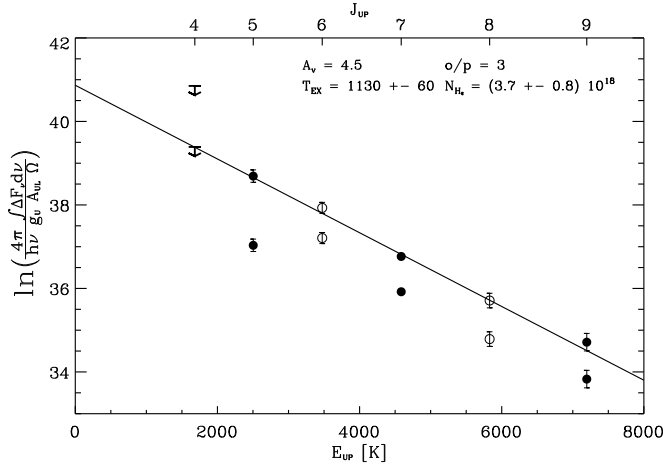


Fig. 6. Rotation diagram for the ortho-H₂ (filled symbols) and para-H₂ (open symbols and upper limit) lines observed toward the flow from SMM 1. Linear regression fits to extinction corrected data is shown by the full drawn line. The physical parameters with their formal errors are given in the figure (see also the text).

how well these assumptions are justified. In the next sections, this will be addressed by employing first a method based on the Sobolev approximation and then a full Monte

Carlo calculation, including gradients for both density and temperature. The latter method takes any (previously neglected) beam dilution effects directly into account.

4.2.2. Large Velocity Gradient models: CO

In the Large Velocity Gradient model (LVG) opacity effects in the lines are explicitly taken into account by introducing the photon escape probability formalism. Crudely speaking, the critical density of the transition, $n_{\text{crit}} = A_{\text{ul}}/C_{\text{ul}}(T)$, can be lowered by means of an effective Einstein-probability, $A_{\text{ul}}\beta_{\text{esc}}$, where β_{esc} is in the range 0 to 1 for infinite and zero optical depth, respectively.¹ This can effectively ‘delay’ line saturation. For illustrating purposes, $\beta_{\text{esc}} \sim 1/\tau_{\text{line}}$ but, in general, β_{esc} is geometry dependent (Castor 1970).

For under-resolved sources, an ambiguity can arise from the fact that hot and tenuous models may be indistinguishable from cool and dense ones. However, assuming that the rotation diagram analysis can provide an estimate of the kinetic gas temperature, LVG can be used to determine the average density of the emitting region. This is shown in Fig. 8, for the resulting $\log n(\text{H}_2) = 6.2 \pm 0.2$

¹ The collision rate coefficients for CO, C_{ij} , have been re-evaluated and extended to higher J values in Appendix B.

Table 5. OH line measurements in the spectrum of SMM 1

$^2\Pi$ Transition		Wavelength (μm)			Flux $\times 10^{19}$ (W cm^{-2})	Err $\times 10^{19}$ (W cm^{-2})	Single/ Multi fit	LWS Detector			
$\Omega - \Omega'$	$J - J'$	λ	λ_{obs}	$\Delta\lambda$	σ_λ	F	ΔF				
$1/2 - 1/2$	$3/2 - 1/2$	163.26	163.26	Fix	+0.00	0.60	Fix	1.39 ± 0.90	0.93	S	LW 5
			163.26	Fix	+0.00	0.60	Fix	1.00 ± 0.85	0.91	S	LW 4
$3/2 - 3/2$	$5/2 - 3/2$	119.34	119.38 ± 0.20	+0.04	1.31 ± 0.11	2.07 ± 0.49	0.56	S	LW 2		
			119.42 ± 0.07	+0.08	0.60	Fix	1.28 ± 0.22	0.36	S	LW 2	
$3/2 - 3/2$	$7/2 - 5/2$	84.51	84.43 ± 0.03	-0.08	0.39 ± 0.03	2.94 ± 0.64	0.79	S	LW 1		
			84.44 ± 0.08	-0.07	0.60	Fix	3.49 ± 0.73	0.87	S	LW 1	
			84.51 ± 0.02	+0.00	0.41 ± 0.02	4.02 ± 0.50	0.58	S	SW 5		
			84.50 ± 0.02	-0.01	0.29	Fix	3.26 ± 0.31	0.42	S	SW 5	
$1/2 - 3/2$	$1/2 - 3/2$	79.15	79.14 ± 0.02	-0.01	0.29 ± 0.02	2.84 ± 0.38	0.54	S	SW 5		
			79.14 ± 0.02	-0.01	0.29	Fix	2.86 ± 0.21	0.43	S	SW 5	
			79.17 ± 0.07	+0.02	0.56 ± 0.07	2.22 ± 0.80	0.89	S	SW 4		
			79.14 ± 0.04	-0.01	0.29	Fix	1.47 ± 0.34	0.51	S	SW 4	
$3/2 - 3/2$	$9/2 - 7/2$	65.21	65.18 ± 0.03	-0.03	0.24 ± 0.03	1.51 ± 0.45	0.47	S	SW 3		
			65.18 ± 0.03	-0.03	0.29	Fix	1.64 ± 0.26	0.30	S	SW 3	
$3/2 - 3/2$	$11/2 - 9/2$	53.30						0.73	S	SW 2	

Note to the table: λ is an average wavelength for the various fine structure lines.

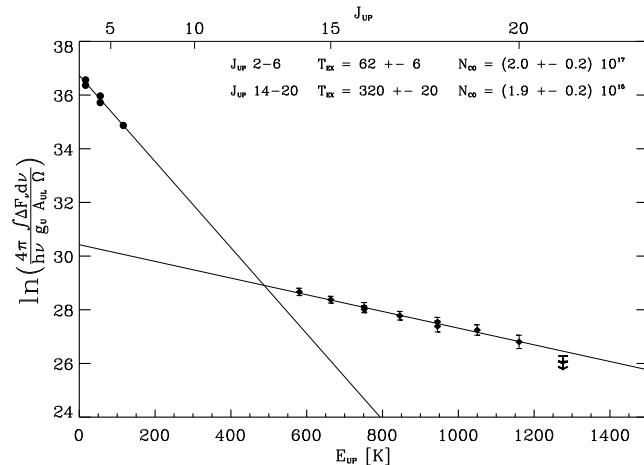


Fig. 7. Rotation diagram for the CO lines observed with the LWS (diamonds, this work) and for ground based data (filled circles), taken from Davis et al. (1999), Hogerheijde et al. (1999) and White et al. (1995). More than one LWS-value for the same upper energy E_u/k refer to measurements with different detectors. The data have been (ad hoc) fit by two linear segments, the solutions of which are given in the figure (see also the text).

cm^{-3} , which is in good agreement with the results by McMullin et al. (2000).

In these models, the presence of a diffuse radiation field is introduced by the dust temperature $T_{\text{dust}} = 40 \text{ K}$, the wavelength of unit optical depth $\lambda_{\tau=1} = 200 \mu\text{m}$, the frequency dependence of the dust emissivity $\beta = -1$ and a geometrical covering factor of 0.5 (cf. Larsson et al. 2000). The (clearly detected) high- J lines are all only mildly sub-thermally excited (justifying a posteriori our initial assumption), but have substantial opacity, e.g.

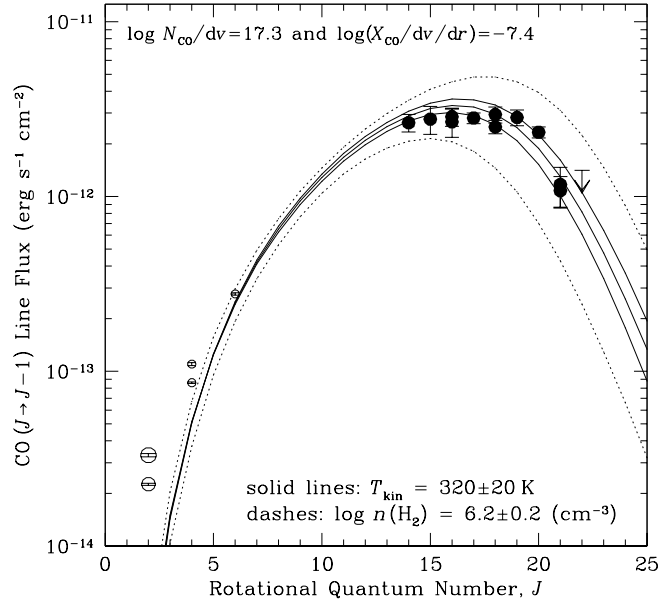


Fig. 8. The fluxes of rotational lines of CO, observed with the LWS, are compared to LVG model computations. Filled circles with error bars refer to LWS data, where more than one value for a given J correspond to different detectors. The upper limit is 3σ . In addition, open symbols represent ground based data, where the different sizes refer to different telescope beams (see Fig. 7). The physical parameters of the LVG model are indicated in the figure.

$\tau_{0(J=14-13)} = 1.7$. First at $J_u = 22$ start the lines to become optically thin again ($\tau_{0(J=22-21)} = 0.14$).

The principle parameter of the LVG model is related to the ratio of the column density to the line width, $N/\Delta v$.

For a given density of the collision partners, $n(\text{H}_2)$, this ratio is given by

$$\frac{N_{\text{CO}}}{\Delta v} \propto X_{\text{CO}} / \frac{\partial v}{\partial r} \quad (3)$$

where the right hand side is the ‘LVG-parameter’. There, $\partial v / \partial r$ is the (Doppler) velocity gradient in the gas and X_{CO} is the molecular abundance relative to H_2 . From Eq. (3), it is clear that LVG models are, in general, not unique, since an increase of the column density could have the same effect as a decrease of the line width.

From the model fit, $N(\text{CO}) = 1.5 \times 10^{18} \text{ cm}^{-2}$ for the adopted $\Delta v = 7.5 \text{ km s}^{-1}$ (FWHM of a Gaussian line shape; see Sect. 4.3). A circular source would have a diameter of about $5''$ (1500 AU), a thickness of about 600 AU and an H_2 mass of about $0.01 M_{\odot}$ (for $X_{\text{CO}} = 10^{-4}$). Finally, the total CO cooling rate amounts to $3.6 \times 10^{-1} L_{\odot}$.

The hot regions emitting in the H_2 lines (Sect. 4.2.1) are not expected to contribute significantly to the CO emission observed with the LWS. We predict the strongest CO lines from this gas to be the ($J = 4 - 3$) and the ($J = 5 - 4$) transitions, with ‘LWS’-fluxes from a $10''$ source of about $1 \times 10^{-14} \text{ erg cm}^{-2} \text{ s}^{-1}$.

4.2.3. LVG models: ^{13}CO , H_2O and OH

The CO-model of the previous section can be used (by keeping $\partial v / \partial r$ constant) to investigate whether it is applicable also to other molecular species. Such a ‘one-size-fits-all’ model would have the advantage of permitting the straightforward estimation of the relative abundance of these species (see Liseau et al. 1996b for an outline of this method). The reasonably satisfactory result of such computations for ^{13}CO , ortho- H_2O , para- H_2O and OH is presented in Fig. 9.

The ^{13}CO spectrum has been computed under the assumption that $^{12}\text{CO}/^{13}\text{CO}$ is as low as 40 (Leung & Liszt 1976). The data are clearly consistent with this value, but the S/N is insufficient to conclusively provide a better defined value. Since the ^{13}CO lines are all optically thin, the cooling in these lines ($1.3 \times 10^{-2} L_{\odot}$) is relatively more efficient than that in CO (by almost a factor of two).

The H_2O model is based on considering 45 levels for both ortho- and para- H_2O , including 164 transitions each. The radiative rates are from Chandra et al. (1984) and the scaled collision rates from Green et al. (1993). The model fit of the observed spectrum requires an $o/p = 3$ for H_2O and the derived H_2O -abundance is $X(\text{H}_2\text{O}) = 1 \times 10^{-5}$. As expected, the excitation is sub-thermal and the lines are very optically thick (e.g., $\tau_{0(\text{o} 179.5 \mu\text{m})} = 433$, $\tau_{0(\text{p} 101 \mu\text{m})} = 218$). Both the 380 GHz ortho-transition ($4_{14} - 3_{21}$) and the 183 GHz para-transition ($3_{13} - 2_{20}$) are predicted to be masing ($\tau_0 = -1$). The total cooling rate due to water vapour is $L(\text{H}_2\text{O}) = 2.1 \times 10^{-1} L_{\odot}$, i.e. at the 60% level compared to the CO cooling rate.

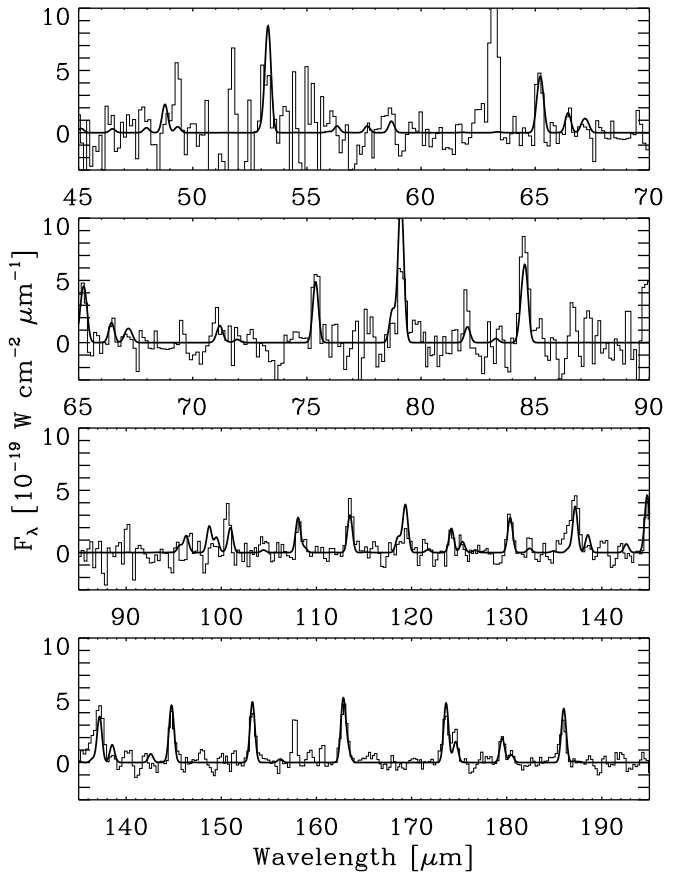


Fig. 9. The fit (smooth line) of the LVG model to the observed spectrum (histogram). All molecules, i.e. CO, ^{13}CO , ortho- H_2O , para- H_2O and OH, are assumed to share the same density and temperature, viz. $n(\text{H}_2) = 1.6 \times 10^6 \text{ cm}^{-3}$, $T_{\text{kin}} = 320 \text{ K}$; for further model details, see the text. Line identifications are as those given in Fig. 4.

For OH, the Einstein A values were computed from the data provided by D. Schwenke², who also gives the energy levels. The collision rate coefficients for 50 transitions were obtained from Offer et al. (1994). Since rates are available for collisions with both ortho- H_2 and para- H_2 , the total rate was based on $\text{H}_2\text{-o/p} = 1$. As before, the excitation is sub-thermal and the lines are optically thick (e.g., $\tau_{0(119 \mu\text{m})} \sim 170$ in each line of the doublet). This refers to the derived, relatively high, value of the OH-abundance of $X(\text{OH}) = 2 \times 10^{-6}$ ($\text{OH}/\text{H}_2\text{O} = 0.2$). The OH lines cool the gas as efficiently as H_2O , viz. $L(\text{OH}) = 2.0 \times 10^{-1} L_{\odot}$. The model is overpredicting the $119 \mu\text{m}$ line flux (whereas the $113 \mu\text{m}$ H_2O line is underpredicted), perhaps indicating a distribution of temperatures (and densities). However, these lines fall in one of the least well performing LWS detectors (LW 2) and instrumental effects cannot be excluded.

Anyway, we have so far considered only models of a homogeneous source at a single kinetic temperature in a plane-parallel geometry. The relaxation of these, likely unrealistic, assumptions is the topic of the next sections.

² Available at <http://george.arc.nasa.gov:80/~dschwenke/>

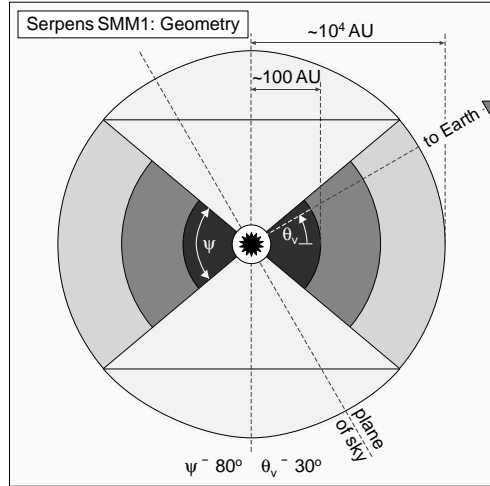


Fig. 10. Model geometry of the dusty torus of SMM 1 (see Sects. 4.2.4 and 4.2.5). Different shades of gray show schematically the density falling off outwards. The radius of the compact dense torus is ~ 100 AU, whereas the outer radius of the envelope is based on our maps.

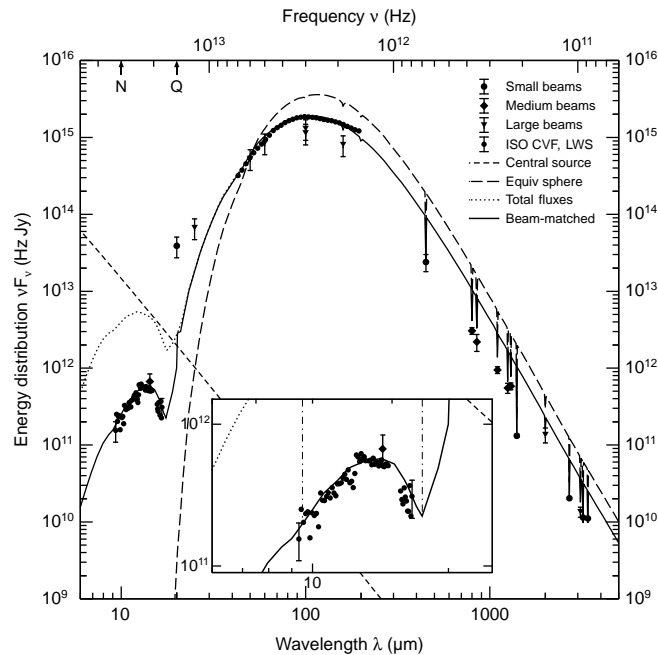


Fig. 11. Comparison of the observed SED of SMM 1 and the model of the dusty torus. The individual fluxes (see Larsson et al. 2000 for details) are labelled by different symbols, to distinguish between beams of different sizes. The model assumes that we observe the torus at an angle of 31°, relative to its midplane. The effect of beam sizes is shown by the vertical lines and by the difference between the dotted and solid lines in the model SED at mid-IR wavelengths. Whereas only the lower points of the vertical lines are relevant, we have connected them to the adjacent continuum by straight lines, to better visualise the effect. The SED for the equivalent spherical envelope is also shown, to illustrate the influence of the bipolar outflow cavities.

Table 6. Main input parameters of the dusty torus model

Parameter	Value
Distance	310 pc
Central source luminosity	$140 L_\odot$
Stellar effective temperature	5000 K
Torus opening angle	80°
Viewing angle	31°
Torus dust melting radius	2 AU
Torus outer boundary	$1.4 \cdot 10^4$ AU
Torus total mass (gas+dust)	$33 M_\odot$
Density at melting radius	$2.5 \cdot 10^{-13} \text{ g cm}^{-3}$
Density at outer boundary	$1.4 \cdot 10^{-18} \text{ g cm}^{-3}$
Outflow visual τ_v	71
Midplane τ_v	2200

4.2.4. 2D radiative transfer model of the dusty torus

In our previous paper, we presented a self consistent radiative transfer model for the SED of SMM 1 (Larsson et al. 2000). For a simplified analysis and for a direct comparison with previous spherical models of the object, we adopted spherical geometry of the dusty envelope. The model provided a good fit to the observations longward of about $60 \mu\text{m}$, but resulted in too low fluxes in the mid-IR. As already noted in that paper, the spherical symmetry may not be a very good assumption for SMM 1, the source driving the bipolar outflow. In this paper, we performed detailed modelling of the dusty object using our 2D radiative transfer code (Men'shchikov & Henning 1997), which enabled us to quantitatively interpret existing dust continuum observations and to derive accurate physical parameters of SMM 1. In the next section, the density and temperature structure of the model will be used in a Monte-Carlo calculation of the CO line radiation transfer in the envelope. Our approach and the model geometry are very similar to those for two other embedded protostars: HL Tau (Men'shchikov et al. 1999) and L1551 IRS 5 (White et al. 2000); we refer to the papers for more details on the general assumptions, computational aspects, and uncertainties of the modelling.

The model assumes that SMM 1 consists of an axially-symmetric (quasi-toroidal), dense inner core surrounded by a similarly-shaped 'envelope' (Fig. 10). A biconical region of much lower density with a full opening angle of 100° is presumed to be excavated in the otherwise spherical envelope by the outflow from SMM 1. The structure, for brevity called 'torus', is viewed at an inclination of 30° with respect to the equatorial plane of the torus. Main input model parameters are summarised in Table 6.

As very little is known about dust properties in SMM 1, we adopted a dust model very similar to that applied by Men'shchikov & Henning (1999) for HL Tau and by White et al. (2000) for L1551 IRS 5. The dust population consists of 4 components: (1) large dust particles of unspecified composition, with radii $100\text{--}6000 \mu\text{m}$, (2) core-mantle

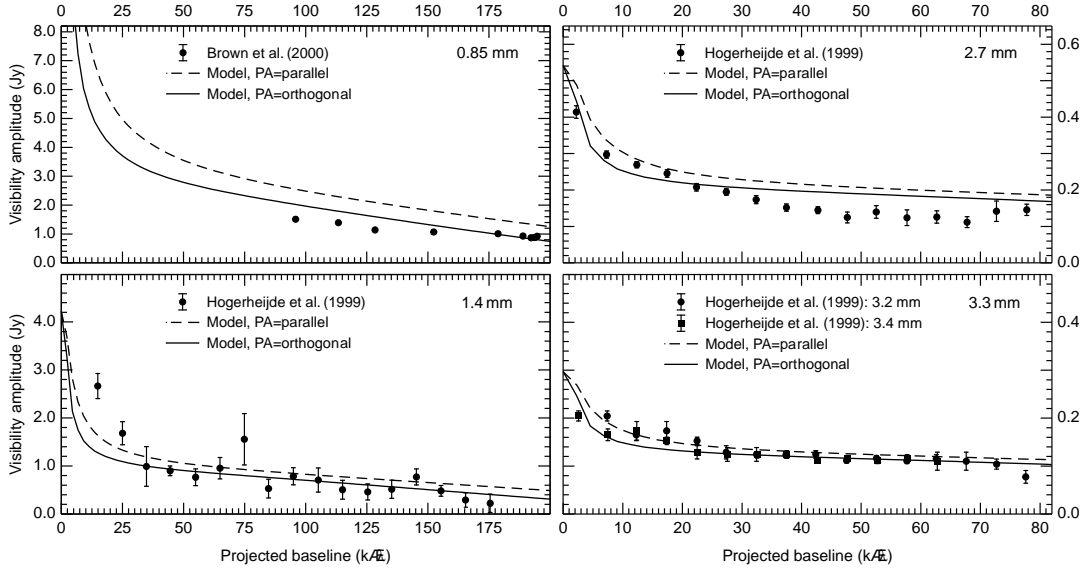


Fig. 12. Comparison of the model visibilities at 0.8 mm, 1.4 mm, 2.7 mm, and 3.3 mm with available measurements of Brown et al. (2000) and Hogerheijde et al. (1999). The upper and lower curves in each panel show the visibilities for two directions in the plane of sky, parallel and orthogonal to the projected axis of the model.

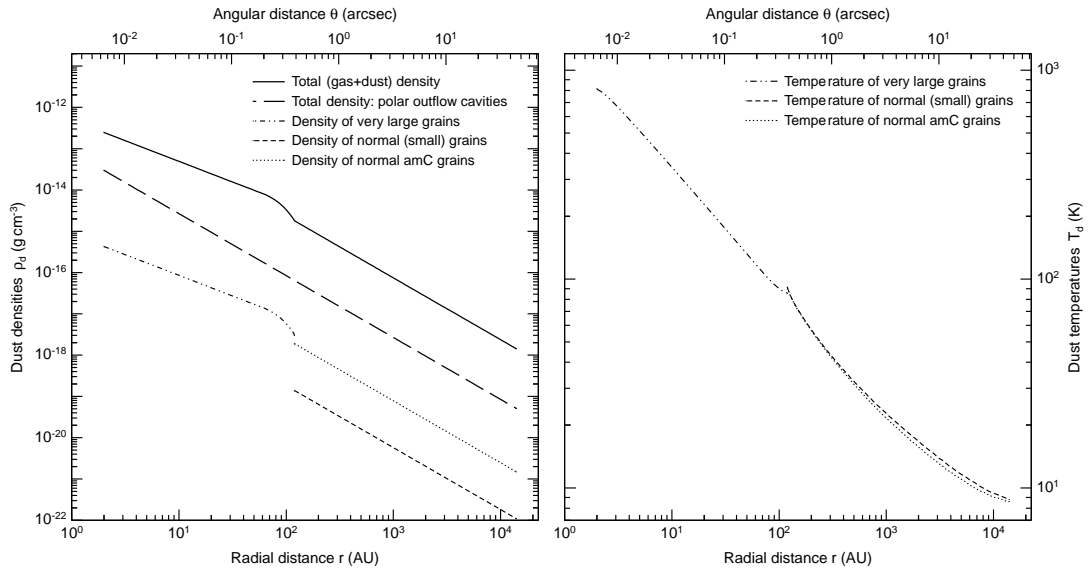


Fig. 13. Density and temperature structure of the model torus of SMM 1. *Left panel:* The total densities in the midplane and in polar outflow regions, and dust densities of different dust grain components (for only their smallest sizes). *Right panel:* The temperature profiles correspond to the midplane of the torus; they were obtained self-consistently from the equation of radiative equilibrium.

grains made of silicate cores, covered by dirty ice mantles, (3) amorphous carbon grains, and (4) magnesium-iron oxide grains. The latter 3 components of dust grains have the same radii of $0.08\text{--}1\,\mu\text{m}$. The dust-to-gas mass ratios of the components are 0.01, 0.0005, 0.0068, and 0.0005, respectively. The first component of very large grains is present only in the compact dense torus ($r \leq 120\,\text{AU}$), where all smaller grains are assumed to have grown into the large particles. Note that although unknown properties of dust generally introduce a major uncertainty in the

derived model parameters, extremely high optical depths in SMM 1 make the model results not very sensitive to the specific choice of the grain properties, except for the presence of very large grains in the dense central core.

In the modelling of the dusty torus, we fitted all available photometry of SMM 1, paying special attention to the effect of different beam sizes. Important constraints for the density structure were provided by the available submm and mm interferometry of the object. The model SED, compared to the observations in Figs. 11, fits almost

every single individual flux in the entire range from the mid-IR to mm wavelengths. Note that it would be wrong to fit the observed data with the total model fluxes, because the angular size of SMM 1 is generally much larger than the photometric apertures. In fact, the model demonstrates that the effect of beam sizes on the fluxes may be as large as an order of magnitude.

Comparison of the model visibilities to the interferometry data shown in Fig. 12 demonstrates that the model is also consistent with the observed spatial distribution of intensity. The visibilities indicate that there is a dense core inside of a lower density envelope. The radial density and temperature profiles of the model, are shown in Fig. 13. The innermost dense core has a $\rho \propto r^{-1}$ density gradient in the model, whereas the outer parts of the lower-density envelope have a steeper density distribution ($\rho \propto r^{-1.5}$). The temperature distribution was obtained in iterations as a solution of the energy balance equation.

4.2.5. 2D radiative transfer of the molecular emission

We have used the density and temperature distributions of this dusty torus model in combination with a Monte Carlo scheme to compute the radiative transfer of the CO lines, and its isotopomers, through the source.

Observations of the Serpens cloud core in the $J = 2 - 1$ transitions of the CO-isotopomers C^{18}O and C^{17}O are present in the archive of the James Clerk Maxwell Telescope (JCMT). These potentially optically thin lines could trace the embedded core SMM 1. Our disk model reproduces the observed line intensities of these low- J isotopomers fairly well (Fig. 14). There, the averaged background emission of the surrounding gas has been subtracted, in order to reveal the line profiles of SMM 1 itself. From the figure it is evident that the C^{18}O and C^{17}O lines are optically thick out to a point, where the temperature falls below 15 K and where substantial condensation of the CO gas onto dust grains occurs. This CO freeze-out was treated following Sandford & Allamandola (1993 and references therein), where the ice-to-gas ratio η is proportional to the dust density n , and to functions of the gas and dust temperatures, T_g and T_d respectively, viz.

$$\eta \propto n T_g^{1/2} e^{1/T_d} \quad (4)$$

In the inner ('core') regions, line opacities are very high so that the photons are essentially trapped. Therefore, the excitation temperature of the molecules follows the kinetic temperature of the H_2 gas. Beyond the core, i.e. in the 'torus', τ drops quickly below unity for the high- J lines, but there, the dust starts to contribute significantly to the (small) opacity (Fig. 15).

The CO lines falling into the LWS range are all formed in the inner, hotter parts of the source ($r \ll 10^3$ AU, $T \gg 10^2$ K). This small line forming region is insufficient to produce the observed high- J line fluxes by more than two orders of magnitude. Irrespective of the geometry, we

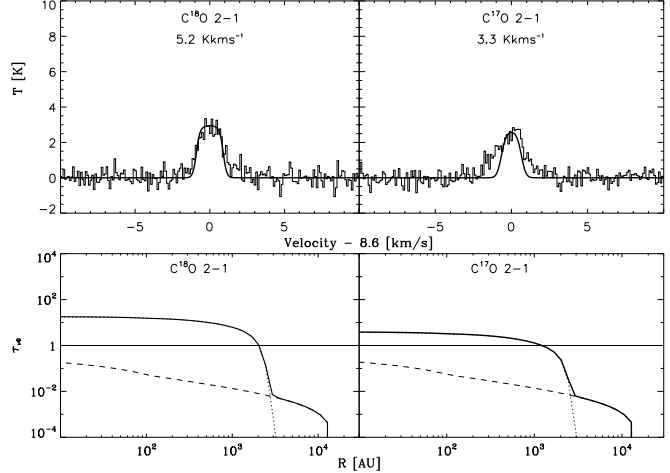


Fig. 14. *Upper panel:* For background emission corrected line profiles of low- J CO isotopomers, viz. C^{18}O (2–1) and C^{17}O (2–1), toward SMM 1 are shown as histograms. The observations were retrieved from the JCMT archive. The results from 2D-Monte Carlo radiative transfer calculations for the disk/torus model are shown by smooth lines. The shown integrated line intensity refers to the model, for which adopted abundances are $^{12}\text{CO}:\text{C}^{18}\text{O}:\text{C}^{17}\text{O} = 1 : 550 : 5$ and freeze-out of the molecules is treated in accordance with the work by Sandford & Allamandola (1993). *Lower panel:* The total line centre optical depth in C^{18}O (2–1) and C^{17}O (2–1), along the line-of-sight toward the central region of the source, is shown by the solid line. Similarly, the dotted lines display the line opacities and the broken lines the dust opacities.

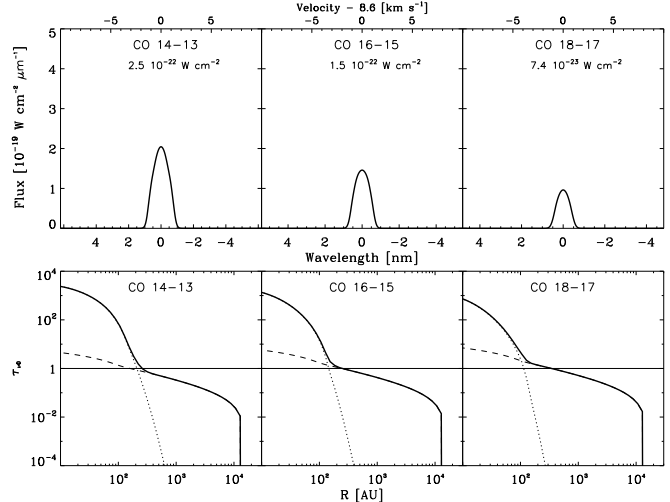


Fig. 15. Same as in Fig. 14, but for three high- J CO transitions, which fall in the ISO-LWS spectral band.

can conclude quite generally that the CO lines observed with the LWS do not originate from the central regions of SMM 1, be it an accretion disk, be it infalling gas (we have also computed 'inside-out' collapse models).

For the excitation of this gas we need to consider alternative mechanisms and, since outflows are known to exist

in this region, shock heating of the gas offers a natural option. Our temperature determinations for the molecular gas (Sect. 4.2.1) are also consistent with this idea.

4.3. Shock heating

From the discussion of the preceding sections we can conclude that the heating of the gas is most likely achieved through shocks. These shocks are generated by flows within the LWS beam. Comparing the observed and predicted molecular line emission with the J-shock models by Hollenbach et al. (1989) and Neufeld & Hollenbach (1994), we find that these models are in conflict with our observations.

In Fig. 16, we compare our observations of rotational lines of H_2 , CO, H_2O and OH with predictions of the C-shock models by Kaufman & Neufeld (1996). The models for $\log n_0 = 5.5$ (cm^{-3}) and $v_s \sim 15 - 20 \text{ km s}^{-1}$ are in reasonable agreement with the for extinction corrected ($A_V = 12$ mag) observed values for H_2 (Kaufman & Neufeld used $o/p = 3$) and for a flux from $6'' \times 6''$ (1 CVF-pixel). For CO, the model fits the observations for an adopted circular source of diameter $11''$. To achieve agreement for H_2O , the model fluxes would need to be adjusted downwards by a factor of 2.5, whereas an increase by more than one order of magnitude (a factor of 12) would be required for OH. Evidently, OH is largely underproduced by these models, a fact also pointed out by Wardle (1999). If on the other hand the Wardle model is essentially correct, this would suggest that the ionisation rate in the Serpens cloud core is significantly higher (up to 10^{-15} s^{-1}) than on the average in dark clouds, $\zeta = (10^{-18} - 10^{-17}) \text{ s}^{-1}$. High X-ray activity is known to be present within the Serpens cloud core (Smith et al. 1999 and references therein). It is conceivable that such a high ionisation rate could also have considerable consequences for the cloud chemistry and its evolution. For instance, a relatively higher H_3^+ abundance could be expected, the effects of which (in addition to the enhanced abundance of OH) may in fact have already been observed (e.g., $\text{HCN}/\text{HNC} \sim 1$; McMullin et al. 2000 and references therein).

4.4. Summarising discussion

Based on their 0.8 mm JCMT-CSO interferometry, Brown et al. (2000) obtained estimates of the size, mass and average (dust) temperature of the disk of SMM1. The estimated mass is larger and the size of the disk is smaller by one order of magnitude than what is required to account for the observed level of line emission (Sect. 4.2.2). Unless the disk (extended atmosphere?) is heated to very much higher temperatures (by an as yet to be identified mechanism) than the 60 K determined by Brown et al., we find it unlikely that the molecular line spectrum of SMM1 is of circumstellar disk origin. Our own calculations (Sect. 4.2.4) confirm this conclusion.

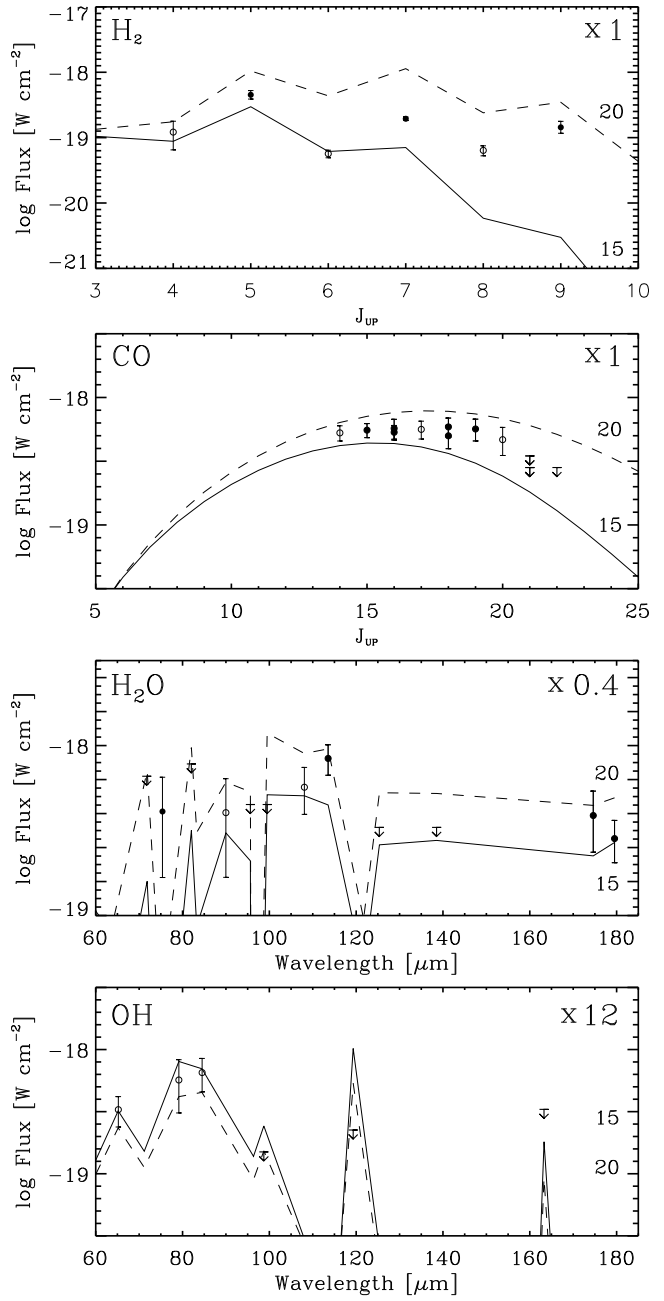


Fig. 16. Comparison of our molecular line observations with the predictions of theoretical models of C-shocks (Kaufman & Neufeld 1996). The pre-shock density is always $\log n_0 = 5.5$ (cm^{-3}). Solid and dashed lines are for models with $v_s = 15 \text{ km s}^{-1}$ and 20 km s^{-1} , respectively. The H_2 models refer to the CVF pixel size, whereas the other panels are for a circular source of diameter $11''$. The scaling factors, necessary to bring the observed and model data into agreement, are indicated in each frame by ‘ \times factor’.

It is intriguing that the luminosity of the spherical model of SMM1 ($71 L_\odot$, Larsson et al. 2000) is close to the ‘magic number’ of the classical main accretion phase of solar mass stars (Shu et al. 1987). At

the elevated cloud temperature of the Serpens cloud core (~ 40 K, White et al. 1995), the isothermal sound speed is 0.4 km s^{-1} and, hence, the (time averaged, cf. Winkler & Newman 1980) mass accretion rate corresponds roughly to $\dot{M}_{\text{acc}} = 10^{-5} M_{\odot} \text{ yr}^{-1}$, yielding $L_{\text{acc}} = 70 L_{\odot}$, where we have used the mass-radius relationship of Palla & Stahler (1990). In this scenario, the age of SMM 1 would be about 10^5 yr or less, depending on the details of the acquired mass of the (presumably deuterium burning) central core. Regarding the data presented in this paper, we find it however difficult to reconcile this accretion shock model with our observations. As concluded in Sect. 4.2.4, the excitation of the observed lines requires significantly larger volumes at elevated densities and temperatures.

The H_2 observations are partially resolved and there exists no ambiguity as to where, with respect to SMM 1, the emission arises (cf. Fig. 2). These lines trace a collimated outflow toward the northwest of SMM 1, which is also seen in ro-vibrationally excited H_2 line emission (Eiroa & Casali 1989; Hodapp 1999). In the graphs of Fig. 16, we have assumed that also the LWS lines originate essentially at the location of the H_2 spots (i.e. we have artificially introduced another factor of two for the fluxes). However, the dereddened data of Eiroa & Casali (with the A_V -value determined in Sect. 4.2.1) could potentially present an additional difficulty for the C-shock model (Kaufman & Neufeld 1996). The estimated 1-0S(1) line intensity would in this case be larger by more than two orders of magnitude than that predicted by the model. We cannot exclude at present, however, the possibility that the 1-0S(1) emission observed by Eiroa & Casali (1989) is essentially unextinguished. Photometrically calibrated data at higher spatial resolution would be required to settle this issue.

The mechanical energy input by the flow is $L_{\text{mech}} = 0.5 \mu_{\text{gas}} m_H n_0 v_s^3 \times \text{area}$, which for a pre-shock density of $\log n_0 = 5.5$, a shock velocity $v_s = (15 - 20) \text{ km s}^{-1}$, and a $5''$ source size yields $L_{\text{mech}} = (6.4 - 15.1) \times 10^{-2} L_{\odot}$. From the Kaufman & Neufeld (1996) C-shock model, this gas is cooled by H_2 at a rate of $(1.0 - 4.7) \times 10^{-2} L_{\odot}$. From the LWS data, we inferred the total cooling rate through the lines of CO, ^{13}CO , H_2O and OH of $78 \times 10^{-2} L_{\odot}$ (Sects. 4.2.2 and 4.2.3), corresponding to 0.5% to 1% of the total dust luminosity. This is larger by factors of 5 to 12 and it is thus not excluded that the shocked regions observed in the H_2 lines and those giving rise to the FIR lines are not the same. We reached the same conclusion on the basis of our excitation and radiative transfer calculations.

The observed and background-corrected $[\text{O I}] 63 \mu\text{m}$ emission toward SMM 1 suggests a contribution also by J-shocks within the LWS beam (Sect. 4.1.2). Intriguingly, the derived dimensions are practically identical to those determined for the LWS-molecular emission, albeit existing J-shock models do not predict the relative intensities correctly. At present, we can merely conclude that shocks, in general, provide a plausible energy input mechanism, although the details of the shock type(s) are less clear. We propose that predominantly slow shock waves in the

dense medium surrounding SMM 1 provide the heating of the molecules we have observed with ISO, whereas dynamical collapse is not directly revealed by our data.

5. Conclusions

Based on spectrophotometric ISO imaging with the LWS and the CAM-CVF of significant parts of the active star forming Serpens cloud core our main conclusions can be summarised as follows:

- We find the emission in the $[\text{O I}] 63 \mu\text{m}$ and $[\text{C II}] 157 \mu\text{m}$ fine structure lines to be extended in our $8' \times 8'$ map. The absolute intensities and their ratios can be explained in terms of PDR models, where a UV field of $G_0 = 15 \pm 10$ is falling onto the outer layers of the dark cloud, where densities are of the order of $(10^4 - 10^5) \text{ cm}^{-3}$.
- Also the emission in rotational lines of H_2O and high- J CO appears (slightly) extended, but we cannot exclude the possibility that it arises from point sources in the field, viz. the Class 0 objects SMM 9/S 68 and SMM 4. The maximum of the emission is observed toward SMM 1, the dominating far infrared and submm source in the Serpens cloud core.
- The spectrum of SMM 1 contains numerous lines of CO, H_2O and OH. These lines are generally subthermally excited and optically thick and trace regions of dimensions $\sim 10^3 \text{ AU}$ ($\sqrt{1500 \times 600} \text{ AU}$), where temperatures are above 300 K and densities above 10^6 cm^{-3} . The derived abundances, relative to H_2 , are for CO, H_2O , OH and ^{13}CO , respectively, $X_{\text{mol}} = (1, 0.1, 0.02, \geq 0.025) \times 10^{-4}$. The ortho-to-para ratio for H_2O is consistent with the high temperature equilibrium value (ratio of the statistical weights of the nuclear spins), i.e. $\text{H}_2\text{O-}o/p = 3$.
- The relatively high OH abundance is indicative of an elevated level of ionising flux in the Serpens cloud core, causing the ionisation rate to be $\zeta \gg 10^{-18} \text{ s}^{-1}$, i.e. significantly higher than the average rate prevailing in dark clouds. Strong and active X-ray sources, known to exist in the cloud, could be responsible for this radiation.
- The observed SED of SMM 1 is consistent with a model of a dusty torus with an outer radius of 14 000 AU ($45''$). The torus is heated by a central stellar source, with a (somewhat arbitrarily) adopted effective temperature of 5000 K. A luminosity of $140 L_{\odot}$ is required to explain the observations. The total mass of the toroidal core of SMM 1 is $33 M_{\odot}$. The derived visual extinction through the torus exceeds 2000 mag and the torus is optically thick up to mm wavelengths.
- 2D modelling of the radiative transfer through the circumstellar torus of SMM 1 reveals that it is highly unlikely that the observed molecular emission arises in the torus. The same conclusion can be drawn for models of dynamical collapse ('inside-out' infall).

- The H₂ data have been obtained at significantly higher spatial resolution than that offered by the LWS. These CAM-CVF observations trace the regions of pure rotational H₂ line emission. The H₂-maxima are observed to be displaced from SMM 1 and are situated toward the northwest, along the jet of outflowing material from this Class 0 source. The temperature of $\sim 10^3$ K of this H₂ gas is indicative of the heating by relatively slow shock waves.
- The comparison of our molecular line data with shock models suggests that shock heating with $v_s \sim (15-20)$ km s⁻¹ along the outflow of SMM 1 is the most likely mechanism of molecular excitation, although the details of these shocks are less clear.

Acknowledgements. We are grateful for the help with the data reductions of the CVF observations by Stephan Ott. We also thank Ewine van Dishoeck for making available to us the collision rate coefficients for OH in electronic form. The support of this work by *Rymdstyrelsen* (Swedish National Space Board) is acknowledged.

Appendix A: Reduction of the LWS data

The photometric calibration of the LWS is primarily based on observations and models of the planet Uranus. The S/N in these observations is rather modest, which will affect the relative spectral response function (RSRF) derived from these data. When calibrating the ‘science data’, the registered photocurrent is divided by the RSRF, propagating any uncertainty in the RSRF, which will ultimately lead to errors in the derived flux density, F_λ .

The derived photocurrent after standard processing, resulting in an SPD file and where identified instrumental peculiarities have been removed, is shown for the LW 5 LWS detector in the upper panel of Fig. A.1, together with the relative spectral response function scaled to the same mean value. From the figure, it is evident that many features seen in the photocurrent are due to the detector and grating response.

The middle panel of Fig. A.1 shows again the photocurrent and the RSRF, but now after the subtraction of a wide boxcar smoothing function (continuum subtraction). The upper curve shows the result of the division of the photocurrent by the response function. This allows us to gauge the effects on the spectra from the narrow features of the RSRF. In the long wavelength regime of the LWS, and in LW 5 in particular, there are spurious absorption features at positions, where the RSRF is steep. In regions, where the RSRF has steep gradients, can already very small wavelength errors create large features that could be mistaken for spectral lines. A wavelength mismatch between the photocurrent and the RSRF will also introduce an overall lowered S/N.

In the lower panel of Fig. A.1, a relative shift by less than a quarter of an resolution element (the original sampling rate was at four times the spectral resolution) of the photocurrent resulted in the considerable reduction of an apparent broad ‘absorption’ feature near 172 μ m, an overall better S/N and therefore a better definition of the spectral lines.

All individual spectra for all ten detectors have been carefully monitored for obviously anomalous features which (most likely) were introduced by the RSRFs. This was done for the

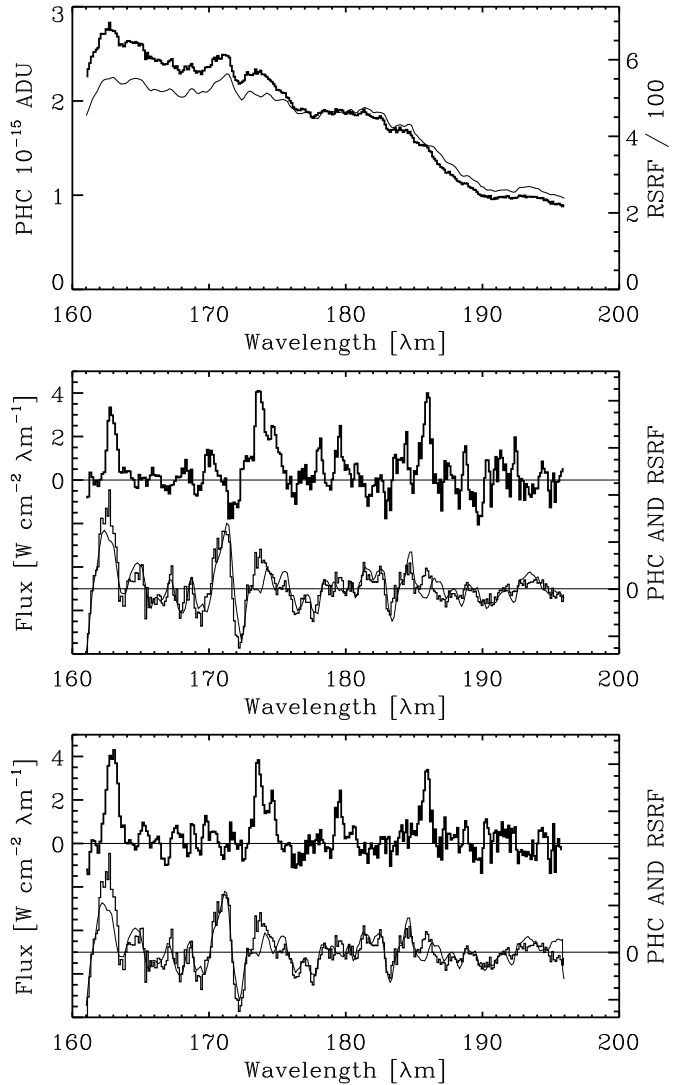


Fig. A.1. Upper panel: The observed wavelength dependence of the photocurrent (thick line) for the detector LW 5 of the LWS. The thin line refers to the grating response function (RSRF) of the detector, scaled to the same mean value as the photocurrent. **Middle panel:** The lower curves are the same as in the upper panel, after subtracting boxcar fits. The division of the photocurrent by the RSRF results in the upper curve, which is the observed flux density (for clarity a median fit to the continuum has been subtracted). **Lower panel:** The same as in the middle panel, but with a small wavelength shift ($< 0.15 \mu\text{m}$) of the observed photocurrent, before division. Evidently, the ‘noise’ is much reduced: compare, e.g., the spurious ‘absorption’ feature near 172 μm in the middle and lower panels.

RSRFs of both OLP 8 and OLP 10 and any such spurious features were, of course, corrected for. This does not guarantee, however, that no such false spectral features do still exist in our data, as we were very restrictive in our application of any wavelength shifts.

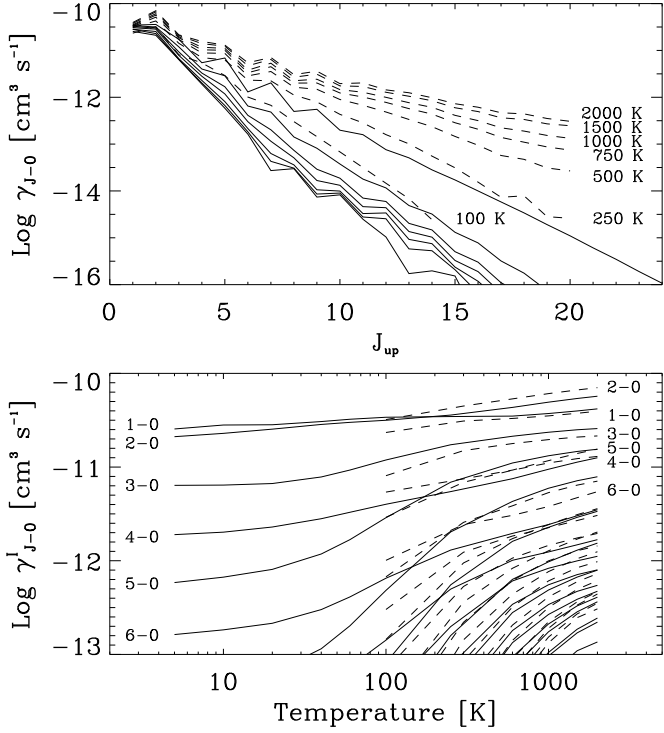


Fig. B.1. Downward rate constants for collisions of CO with para-H₂: **Upper panel:** as a function of J , where the solid lines are for $T = 5, 10, 20, 40, 60, 100$ and 250 K from Flower (2001), and the dashed lines for $T = 100, 250, 500, 750, 1000, 1500$ and 2000 K from Schinke et al. (1985). **Lower panel:** as a function of T_{kin} , with the data by Schinke et al. adjusted to fit those by Flower at 400 K, expanding the rates for the low temperatures to $T = 2000$ K (see the text). These rates are labelled γ^I in the figure.

Appendix B: Collision rates for CO

We used rate coefficients for collisions of CO with H₂ which are based on values found in the literature but which have been extended to rotational quantum numbers $J_u = 40$, although extrapolations to higher J is not excluded.

For $J_u \leq 29$ and for low temperatures, ($5 - 400$) K, we used the recent rates of Flower (2001; ortho-H₂-CO and para-H₂-CO; downward rates). For the higher temperature range of ($> 400 - 2000$) K, the calculations by Schinke et al. (1985; para-H₂-CO; upward rates) were used. The matching between these data sets is roughly acceptable, but there exist disagreements (Fig. B.1), which reflect the differences in assumptions and computational methods (see the discussion of resonances by Flower).

In order to arrive at a consistent set of collision rate constants for the hole range of temperatures, the Schinke et al. data (correctly transformed to de-excitation rates; see also: Viscuso & Chernoff 1988) were laterally shifted to fit the Flower data at 400 K. A satisfactory matching was, however, not really possible for the lowest transitions connecting to the ground state, see the lower panel of Fig. B.1. In the figure, these expanded rates are labelled γ^I .

These γ^I data span J -values up to 20 and temperatures between 400 and 2000 K. For the same temperature intervall,

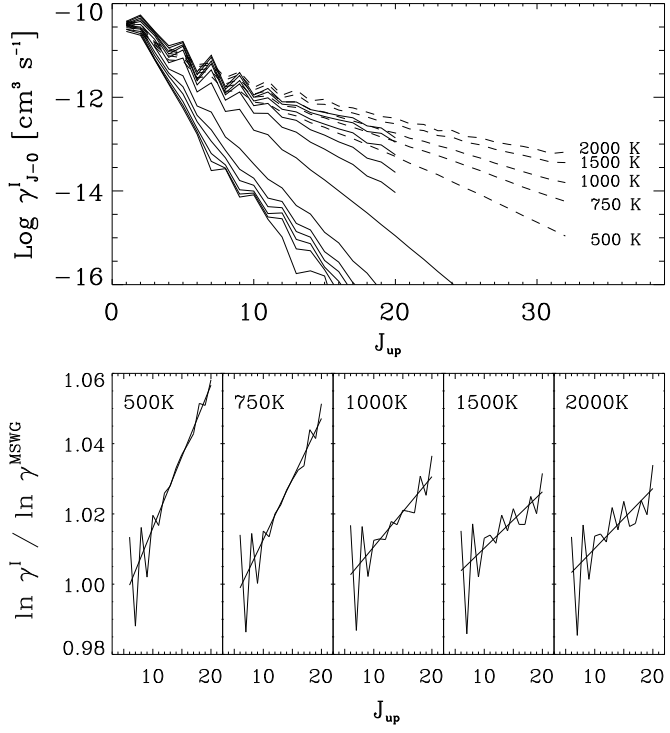


Fig. B.2. Rate constants for CO as a function of J : **Upper panel:** the solid lines refer to the rescaled data of Fig. B.1, i.e. γ^I , whereas the dashes are for $T = 500, 750, 1000, 1500$ and 2000 K from McKee et al. 1982 (collisions with He, scaled to H₂, and up to $J = 32$). **Lower panel:** the fitted ratios of these rates ($J_u \leq 20$) as a function of J_u and, as an example, for the five selected temperatures.

McKee et al. (1982, MSWG) have published calculations (He-CO; downward rates) for J -values up to 32 (Fig. B.2 upper panel). These rates ($\times 1.37$) were divided into the Schinke et al. rates and fit by a polynomial to correct the shape of the McKee et al. data (Fig. B.3 upper panel), viz.

$$\ln \gamma^I / \ln \gamma_{\text{MSWG}} = a + b J \quad 20 \leq J \leq 32 \quad (\text{B.1})$$

to obtain a new set of rate coefficients

$$\gamma^{II} = \gamma_{\text{MSWG}}^{a+bJ} \quad (\text{B.2})$$

For the expansion to $J = 40$, the γ^{II} were fit to a second order polynomial, viz.

$$\ln \gamma^{II} = c + d J + e J^2 \quad 7 \leq J \leq 32 \quad (\text{B.3})$$

the result of which was used for the extrapolations of the para-H₂ rates up to $J = 40$, viz.

$$\gamma^{III} = \exp(c + d J + e J^2) \quad J > 32 \quad (\text{B.4})$$

This provides us finally with the full set of collision rate coefficients for $J_u \rightarrow 0$ for J_u up to 40 (Fig. B.3).

So far, we have considered rates only connecting to the ground state, i.e. $\gamma_{J=0}$. Flower (2001) did provide rates for collision transitions between all level's, but for higher J -values and/or higher temperatures we don't have that information.

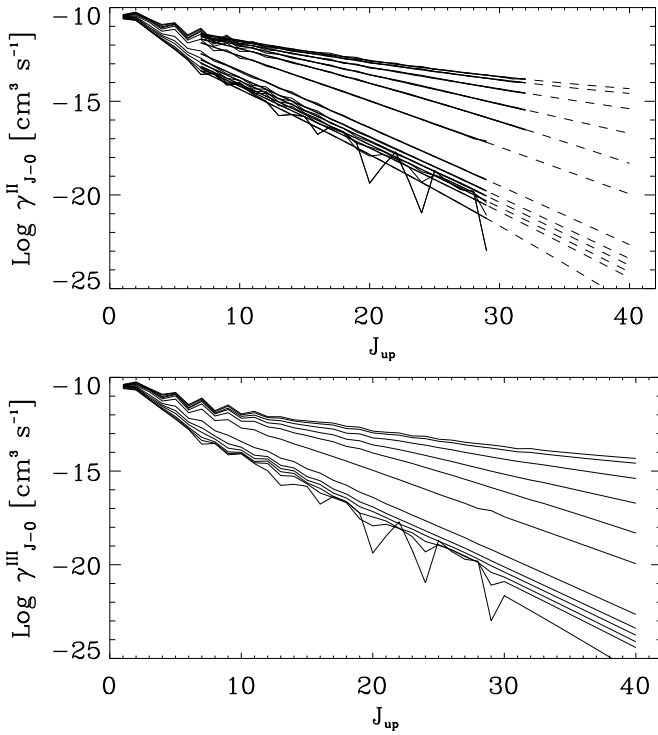


Fig. B.3. Upper panels: Applying the curvature corrections to the data by McKee et al. results in the rates named γ^{II} and shown by the solid lines. The extrapolations of γ^{II} to high J -values are indicated by the dashed lines. **Lower panel:** The finally adopted collision rate coefficients for CO, γ^{III} , for the hole range in temperature, $T = (5 - 2000)$ K, and energy, $J = 0 - 40$.

If the kinetic energy of the collision partners on the other hand is large compared to the rotational energy spacing of the CO molecule, the other rate coefficients can be obtained from (Goldflam et al. 1977; McKee et al. 1982)

$$\gamma_{J-J'} = (2J' + 1) \times \sum_L (2L + 1) \begin{pmatrix} J & L & J' \\ 0 & 0 & 0 \end{pmatrix}^2 A_{L,J}^2 \gamma_{L-0} \quad (B.5)$$

where the Wigner 3- j symbol designates the Clebsch-Gordan coefficients, which were computed exactly (see, e.g., Zare 1986). Further, the factor $A_{L,J}$

$$A_{L,J} = \frac{6 + (aL)^2}{6 + (aJ)^2}, \text{ where } a = 0.13 B_0 l_{\text{sca}} \left(\frac{\mu}{T}\right)^{\frac{1}{2}} \quad (B.6)$$

given by McKee et al. (1982), should correct for the decreased accuracy when the energy splittings become larger. $B_0 = 1.9225 \text{ cm}^{-1}$ is the rotational constant (Lovas et al. 1979), $l_{\text{sca}} = 3 \text{ \AA}$ is a typical scattering length, $\mu = 3.5 \text{ amu}$ is the reduced mass of the colliding CO and He particles and T is the kinetic gas temperature.

Finally, the rates for the inverse transitions were obtained from the condition of detailed balancing, viz.

$$(2J' + 1) \gamma_{J'-J} = (2J + 1) \gamma_{J-J'} \exp(-h \nu_{J-J'}/kT) \quad (B.7)$$

For ^{13}CO , we used the same rate constants as for CO, with the proviso that the mass difference potentially introduces an additional error on the collision rates (3.5%).

References

Abgrall H., & Roueff E., 1989, A&AS 79, 313
 André P., Ward-Thompson D., & Barsony M., 1993, ApJ 406, 122
 Bragg S.L., Brault J.W., & Smith W.H., 1982, ApJ 263, 999
 Brown D.W., Chandler C.J., Carlstrom J.E., et al., 2000, MNRAS 319, 154
 Cameron M., & Liseau R., 1990, A&A 240, 409
 Casali M.M., Eiroa C., & Duncan W.D., 1993, A&A 275, 195
 Castor J.I., 1970, MNRAS 149, 111
 Cesarsky C.J., Abergel A., Agnèse P., et al., 1996, A&A 315, L32
 Chandra S., Varshalovich D.A., & Kegel W.H., 1984, A&AS 55, 51
 Chandra S., Maheshwari V.U., & Sharma A.K., 1996 A&AS 117, 557
 Clegg P.E., Ade P.A.R., Armand C., et al. 1996, A&A 315, L38
 Dame T.M., Ungerechts H., Cohen R.S., et al., 1987, ApJ 322, 706
 Davis C.J., Matthews H.E., Ray T.P., Dent W.R.F., & Richer J.S., 1999, MNRAS 309, 141
 de Lara E., Chavarria-K. C., & López-Molina G., 1991, A&A 243, 139
 Eiroa C., & Casali M.M., 1989, A&A 223, L17
 Eiroa C., Torrelles J.M., Gómez J.F., et al., 1992, PASJ 44, 155
 Flower D.R., 2001, J.Phys. B: At.Mol.Opt.Phys. 34, 1
 Goldflam R., Green S., & Kouri D.J., 1977, J.Chem.Phys. 67, 4149
 Goldsmith P.F., & Langer W.D., 1999, ApJ 517, 209
 Green S., Maluendes S., & McLean A.D., 1993, ApJS 85, 181
 Gregersen E.M., Evans II N.J., Zhou S., & Choi M., 1997, ApJ 484, 256
 Harvey P.M., Wilking B.A., & Joy M., 1984, ApJ 278, 156
 Hodapp K.W., 1999, AJ 118, 1338
 Hogerheijde M.R., van Dishoeck E.F., Salverda J.M., & Blake G.A., 1999, ApJ 513, 350
 Hollenbach D.J., 1985, Icarus 61, 36
 Hollenbach D.J., Chernoff D.F., & McKee C.F., 1989, ESA SP-290, p. 245
 Hollenbach D., & McKee C.F., 1989, ApJ 342, 306
 Kaas A.A., 1999, Ph.D. thesis, Stockholm University
 Kaufman M.J., & Neufeld D.A., 1996, ApJ 456, 611
 Kessler M.F., Steinz J.A., Anderegg M.E., et al., 1996, A&A 315, L27
 Lada C.J., & Wilking B.A., 1984, ApJ 287, 610
 Larsson B., Liseau R., Men'shchikov A.B., et al., 2000, A&A 363, 253
 Leung C.-M., & Liszt H.S., 1976, ApJ 208, 732
 Liseau R., Ceccarelli C., Larsson B., et al. 1996b, A&A 315, L181
 Liseau R., Huldtgren M., Fridlund C.V.M., & Cameron M., 1996a, A&A 306, 255
 Liseau R., Giannini T., Nisini B., et al. 1997, in: Reipurth B. & Bertout C. (eds.), Herbig-Haro Flows and the Birth of Low Mass Stars, p. 111
 Liseau R., White G.J., Larsson B., et al., 1999, A&A 344, 342
 Lovas F.J., Johnson D.R., & Snyder L.E., 1979, ApJS 41, 451
 Mardones D., Myers P.C., Tafalla M., et al. 1997, ApJ 489, 719
 McKee C.F., Storey J.W.V., & Watson D.M., 1982, ApJ 259, 647

McMullin J.P., Mundy L.G., Wilking B.A., et al., 1994, *ApJ* 424, 222

McMullin J.P., Mundy L.G., Blake G.A., et al., 2000, *ApJ* 536, 845

Men'shchikov A.B., & Henning Th., 1997, *A&A* 318, 879

Men'shchikov A.B., Henning Th., & Fischer O., 1999, *ApJ* 519, 257

Neufeld D.A., & Hollenbach D.J., 1994, *ApJ* 428, 170

Nordh L., van Duinen R.J., Sargent A.I., et al., 1982, *A&A* 115, 308

Offer A.R., van Hemert M.C., & van Dishoeck E.F., 1994, *J.Chem.Phys.* 100, 362

Ossenkopf V., & Henning Th., 1994, *A&A* 291, 943

Palla F., & Stahler S.W., 1990, *ApJ* 360, L47

Rodríguez L.F., Curiel S., Moran J.M., et al., 1989, *ApJ* 34, L85

Sandford S.A., & Allamandola L.J., 1993, *ApJ* 417, 815

Schinke R., Engel V., Buck U., Meyer H., & Diercksen G.H.F., 1985, *ApJ* 299, 939

Sharpless S., 1959, *ApJS* 4, 257

Shu F.H., Adams F.C., & Lizano S., 1987, *ARA&A* 25, 23

Smith K., Güdel M., & Benz A.O., 1999, *A&A* 349, 475

Strom S.E., Vrba F.J., & Strom K.M., 1976, *AJ*, 81, 638

Swinyard B.M., Clegg P.E., Ade P.A.R., et al., 1996, *A&A*, 315, L43

Testi L., Sargent A.I., Olmi L., & Onello J.S., 2000, *ApJ*, 540, L53

Viscuso P.J., & Chernoff D.F., 1988, *ApJ* 327, 364

Wardle M., 1999, *ApJ* 525, L101

White G.J., Casali M.M., & Eiroa C., 1995, *A&A*, 298, 594

White G.J., Liseau R., Men'shchikov A.B., et al., 2000, *A&A*, 364, 741

Williams J.P., & Myers P.C., 2000, *ApJ* 537, 891

Winkler K.-H.A., & Newman M.J., 1980, *ApJ* 236, 201

Wolniewicz L., Simbotin I., & Dalgarno A., 1998, *ApJS* 115, 293

Zare R.N., 1986, *Angular Momentum*, J. Wiley & Sons

Ziener R., & Eislöffel J., 1999, *A&A* 347, 565